



Silicon Nitride Creep Under Various Specimen-Loading Configurations

Sung R. Choi
Ohio Aerospace Institute, Brook Park, Ohio

Frederic A. Holland
Glenn Research Center, Cleveland, Ohio

The NASA STI Program Office . . . in Profile

Since its founding, NASA has been dedicated to the advancement of aeronautics and space science. The NASA Scientific and Technical Information (STI) Program Office plays a key part in helping NASA maintain this important role.

The NASA STI Program Office is operated by Langley Research Center, the Lead Center for NASA's scientific and technical information. The NASA STI Program Office provides access to the NASA STI Database, the largest collection of aeronautical and space science STI in the world. The Program Office is also NASA's institutional mechanism for disseminating the results of its research and development activities. These results are published by NASA in the NASA STI Report Series, which includes the following report types:

- **TECHNICAL PUBLICATION.** Reports of completed research or a major significant phase of research that present the results of NASA programs and include extensive data or theoretical analysis. Includes compilations of significant scientific and technical data and information deemed to be of continuing reference value. NASA's counterpart of peer-reviewed formal professional papers but has less stringent limitations on manuscript length and extent of graphic presentations.
- **TECHNICAL MEMORANDUM.** Scientific and technical findings that are preliminary or of specialized interest, e.g., quick release reports, working papers, and bibliographies that contain minimal annotation. Does not contain extensive analysis.
- **CONTRACTOR REPORT.** Scientific and technical findings by NASA-sponsored contractors and grantees.

- **CONFERENCE PUBLICATION.** Collected papers from scientific and technical conferences, symposia, seminars, or other meetings sponsored or cosponsored by NASA.
- **SPECIAL PUBLICATION.** Scientific, technical, or historical information from NASA programs, projects, and missions, often concerned with subjects having substantial public interest.
- **TECHNICAL TRANSLATION.** English-language translations of foreign scientific and technical material pertinent to NASA's mission.

Specialized services that complement the STI Program Office's diverse offerings include creating custom thesauri, building customized data bases, organizing and publishing research results . . . even providing videos.

For more information about the NASA STI Program Office, see the following:

- Access the NASA STI Program Home Page at **<http://www.sti.nasa.gov>**
- E-mail your question via the Internet to **help@sti.nasa.gov**
- Fax your question to the NASA Access Help Desk at 301-621-0134
- Telephone the NASA Access Help Desk at 301-621-0390
- Write to:
NASA Access Help Desk
NASA Center for Aerospace Information
7121 Standard Drive
Hanover, MD 21076



Silicon Nitride Creep Under Various Specimen-Loading Configurations

Sung R. Choi
Ohio Aerospace Institute, Brook Park, Ohio

Frederic A. Holland
Glenn Research Center, Cleveland, Ohio

National Aeronautics and
Space Administration

Glenn Research Center

Acknowledgments

The authors are grateful to R. Pawlik for experimental work during the course of this study. This work was sponsored in part by the Strategic Research Fund Program at NASA Glenn Research Center.

Trade names or manufacturers' names are used in this report for identification only. This usage does not constitute an official endorsement, either expressed or implied, by the National Aeronautics and Space Administration.

Available from

NASA Center for Aerospace Information
7121 Standard Drive
Hanover, MD 21076
Price Code: A03

National Technical Information Service
5285 Port Royal Road
Springfield, VA 22100
Price Code: A03

SILICON NITRIDE CREEP UNDER VARIOUS SPECIMEN-LOADING CONFIGURATIONS

Sung R. Choi
Ohio Aerospace Institute
Brook Park, Ohio 44142

Frederic A. Holland
National Aeronautics and Space Administration
Glenn Research Center
Cleveland, Ohio 44135

SUMMARY

Extensive creep testing of a hot-pressed silicon nitride (NC132) was performed at 1300 °C in air using five different specimen-loading configurations: pure tension, pure compression, four-point uniaxial flexure, ball-on-ring biaxial flexure, and ring-on-ring biaxial flexure. This paper reports experimental results as well as test techniques developed in this work. Nominal creep strain and its rate for a given nominal applied stress were greatest in tension, least in compression, and intermediate in uniaxial and biaxial flexure. Except for the case of compression loading, nominal creep strain generally decreased with time, resulting in a less-defined steady-state condition. Of the four creep models—power-law, hyperbolic sine, step, and redistribution—the conventional power-law model still provides the most convenient and reasonable estimation of the creep parameters of the NC132 material. The data base to be obtained will be used to validate the NASA Glenn-developed design code CARES/Creep (ceramics analysis and reliability evaluation of structures and creep).

INTRODUCTION

Advanced ceramics are candidate materials for high-temperature structural applications in gas turbine engines and heat recovery systems. The two major limitations of these materials, slow crack growth and creep, are generally encountered in high-temperature applications. Slow crack growth (also called subcritical crack growth, fatigue, or delayed failure) of inherent flaws can occur until the critical size for catastrophic failure is attained. At higher temperatures, particularly at lower applied stresses, enhanced creep takes place in the form of permanent deformation and/or damage accumulation, leading to a loss of structural integrity and possibly an eventual rupture of components. Therefore, for higher temperature applications, an accurate determination of creep behavior, including creep and rupture parameters and associated mechanisms, is important for ensuring structural integrity and component life. Creep measurements in tension and compression of ceramic materials show that creep is greater in tension than in compression (refs. 1 to 3). Thus, parameters that are derived from relatively easy flexural testing using the conventional simple beam theory, which assumes the neutral axis to be fixed at the beam center during creep deformation, can be misleading. Most structural components are usually subjected to multiaxial stresses, typically combined with tensile and compressive stresses. Therefore, to accurately predict or estimate creep deformation and rupture of multiaxially stressed components, creep (and rupture) parameters of a material should be determined individually both in tension and in compression.

The immediate objective of the work presented in this report was to develop and conduct extensive creep testing to determine the creep behavior of a silicon nitride under various loading configurations at 1300 °C in air. Hot-pressed silicon nitride (NC132, Norton Advanced Ceramics, Northboro, MA, 1990) containing magnesium oxide as the primary sintering aid was chosen as the test material. Over several decades, NC132 has shown a controlled uniformity in mechanical and physical properties such as hardness, fracture toughness, strength, and slow crack growth. In addition, the material has exhibited a moderate-to-high susceptibility to slow crack growth and creep at temperatures greater than 1100 °C (refs. 4 and 5), which is ideal for modeling slow crack growth and creep under various specimen-loading configurations. The loading configurations used in this study include pure tension, pure compression, four-point uniaxial flexure, ball-on-ring biaxial flexure, and ring-on-ring biaxial flexure. For each loading

configuration, five or six applied stresses were used and creep displacements were determined as a function of time for a given applied load.

NASA Glenn Research Center developed an analytical methodology and an integrated design program known as ceramics analysis and reliability evaluation of structures and creep (CARES/Creep) to predict the creep deformation and rupture life of structural ceramic components (refs. 6 and 7). This program consists of two modules and is currently customized to run a postprocessor to a finite-element code (ANSYS, Inc.). The first module is a parameter estimation program used to compute the primary creep parameters based on the time-hardening rule, the steady-state parameters based on the appropriate law (Norton's, hyperbolic sine, or exponential law), and the creep rupture parameters based on the modified Monkman-Grant criterion (ref. 8). In the future, the creep data base generated from this ongoing experimental work will be used to verify the newly developed CARES/Creep code. This will be done by predicting creep deformation of test specimens subjected to multiaxial stresses on the basis of pure tension and pure compression data.

EXPERIMENTAL PROCEDURES

The material used in this work was characterized previously as a candidate gas turbine material to determine fatigue-life prediction parameters (refs. 4, 9, and 10). The microstructure of NC132 typically consists of fine, equiaxed grains of an average size of about 1 μm (fig. 1). All test specimens (except those used for compression) were cut to be perpendicular to the hot pressing direction so that the prospective tensile stress of the specimens would be normal to the pressing direction. In contrast, the compression test specimens were cut to be parallel to the pressing direction. Test specimens were cut from a 25- by 25-cm by 13-mm billet, where the thickness (13 mm) direction corresponded to the pressing direction. All test specimens were annealed in air for 20 h at the test temperature of 1300 $^{\circ}\text{C}$. The major physical and mechanical properties of NC132 silicon nitride determined from previous studies by the bulk-mass method (S.R. Choi, 1997, NASA Glenn Research Center, Cleveland, OH, Elevated Temperature Slow Crack Growth Testing of a Silicon Nitride in Uniaxial and Biaxial Flexure Loading Conditions, unpublished) are as follows:

Density, g/cm^3	3.20
Young's modulus, ^a E , GPa	315
Hardness, ^b GPa	16.53
Poisson's ratio, ^a	0.30
Fracture toughness, ^c $\text{MPa}\cdot\text{m}$	4.64 ± 0.42
Room temperature strength, ^d MPa	688 ± 129
Slow crack growth parameters ^e	
n26
D	750

^a By the impulse excitation method, American Society for Testing and Materials (ASTM) C1259 (ref. 11).

^b By the Vickers microhardness method, ASTM C1327 (ref. 12).

^c By the SEPB method, ASTM C1421 (ref. 13).

^d Four-point flexure testing, ASTM C1161 (ref. 14).

^e By the constant stress-rate flexure test method, ASTM C1368 (ref. 15).

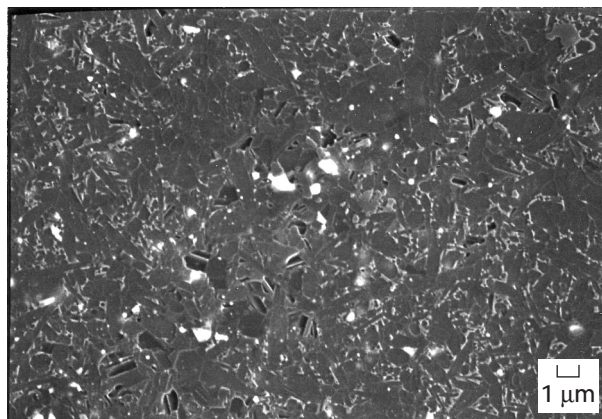


Figure 1.—Microstructure of NC132 silicon nitride.

TESTING

Testing was performed at 1300 °C in air. The five specimen-loading configurations used in the creep testing are depicted in figure 2. All of the test specimens with some preload, depending on the type of loading, were kept at the test temperature for thermal equilibration for about 20 min prior to testing.

Tension Creep Testing

For pure tension tests, dogbone-shaped, pin-loaded tension specimens with round cross sections were used and were nominally 2.0 mm in diameter, 70 mm in length, and 20 mm in gauge length. A schematic of the tension test specimen is shown in figure 3. The choice of round-gauge cross section was intended to minimize any stress concentration that might occur due to bending by misalignment in tension specimens with square cross sections. Specimens with round cross sections were satisfactorily used previously in strength and fatigue testing of alumina at ambient temperature (ref. 16). The pin holes in the tension test specimens were also tapered so that a load could be applied to the center of the specimen with minimum misalignment, as already suggested (ref. 17). Some of the as-machined specimens exhibited chatter and/or spiral marks in the gauge section as well as a discontinuity in the transition region between the gauge and the neck sections. This undesirable machining, also observed previously in specimens with square cross sections (ref. 18), was remedied by careful polishing with fine silicon carbide (SiC) paper and fine diamond paste. It should be noted that in contrast to strength testing, rigorous specimen or surface preparation is not necessary in creep testing, where relatively low applied stresses are employed.

Each tensile creep test specimen was loaded through SiC (Hexoloy, Carborundum Corp., Niagara Falls, NY) 5-mm-diameter loading pins with SiC pull rods (Cryster, Carborundum Corp., Niagara Falls, NY) using a dead-weight tensile creep tester (Applied Test Systems, Inc. (ATS), Butler, PA) (fig. 4). For creep deformation measurements, two Hexoloy SiC flags were attached to the gauge section of each test specimen by friction (ref. 17) so that the actual gauge length was the distance between any two selected lines in the flags. The gauge lengths used here ranged from 12 to 15 mm. To ensure a minimum misalignment with bending strain of less than 5 percent as

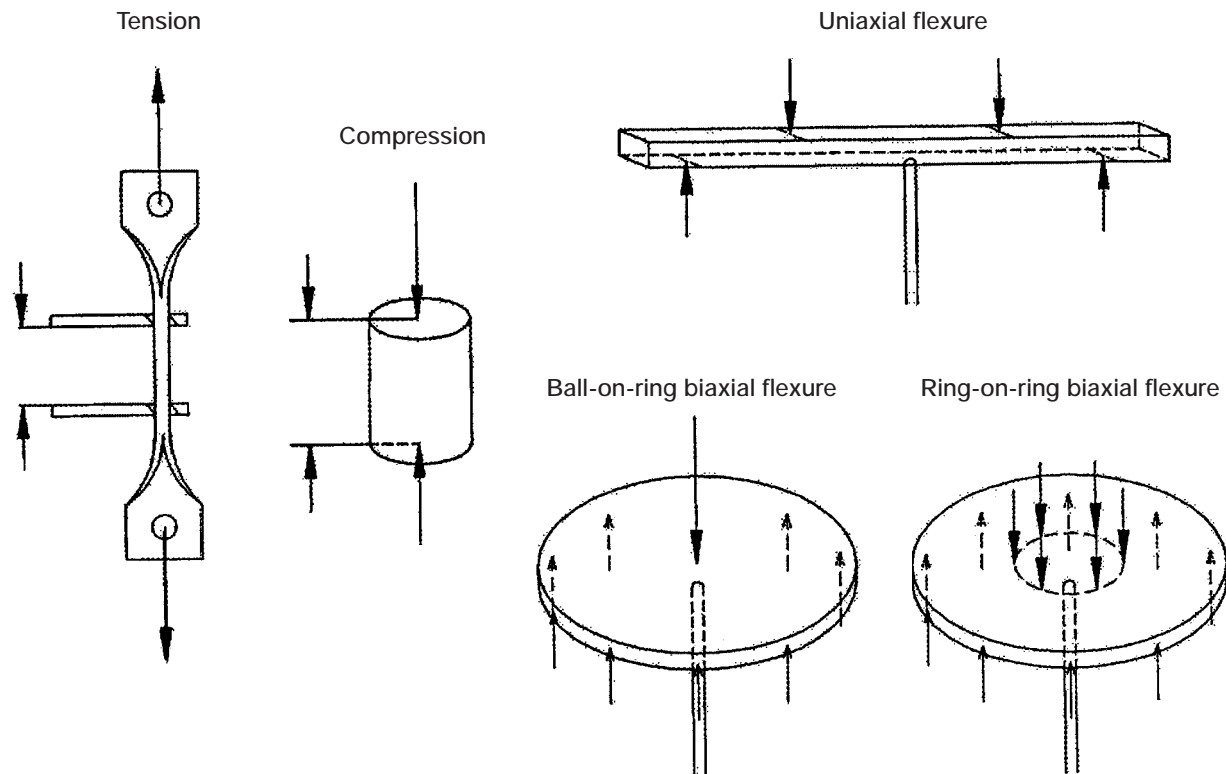


Figure 2.—Five creep specimen-loading configurations used in study.

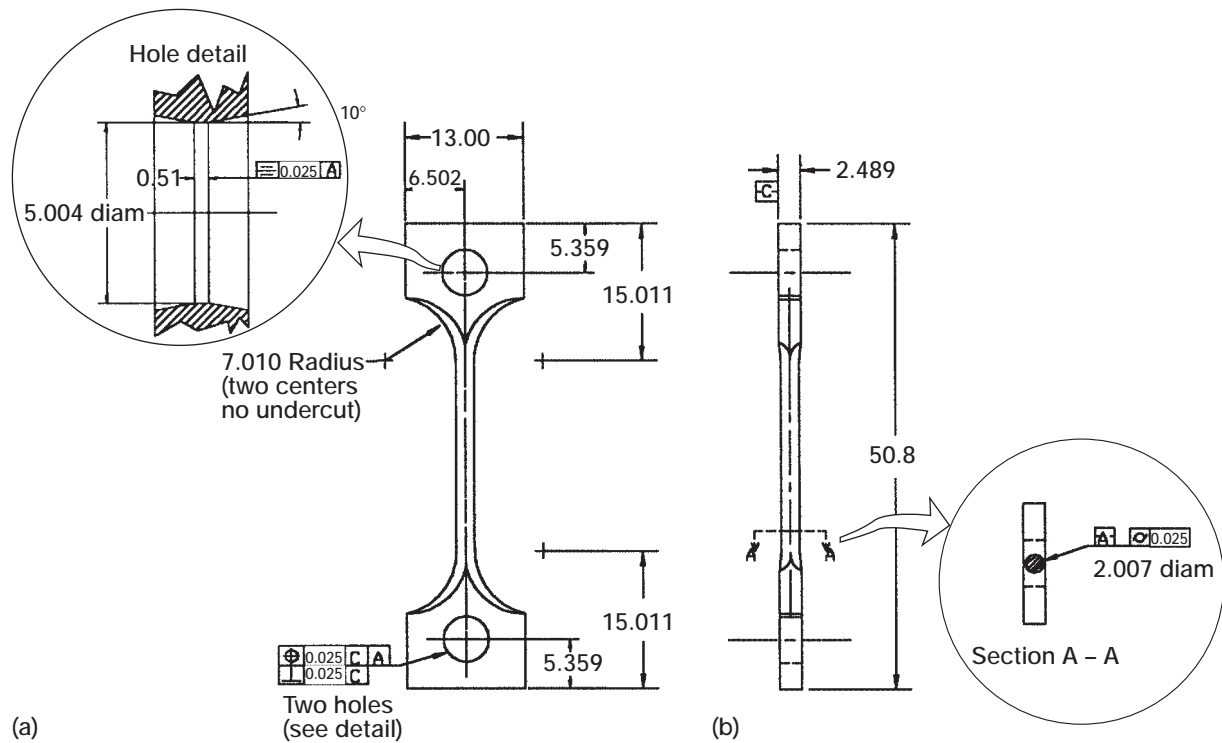


Figure 3.—Tension creep test specimen. All dimensions given in millimeters. (a) Front view. (b) Side view.

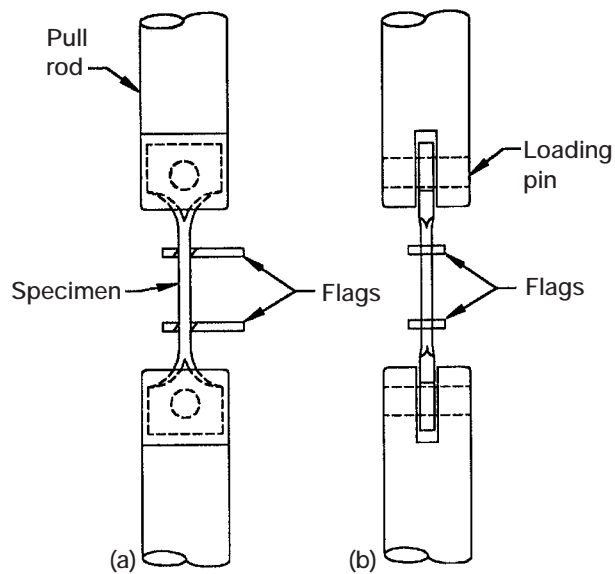


Figure 4.—Test setup in tension creep testing.
(a) Front view. (b) Side view.

specified in the American Society for Testing and Materials (ASTM) Test Method C1291 (ref. 19), misalignment was checked and adjusted within the specification with a strain-gauged reference specimen. Creep displacements were monitored using a scanning laser extensometry system (Beta LaserMike, Dayton, OH). The scanning laser beam was interrupted by the flags, thus defining the distance at any instant of time between the flags. The change in the distance corresponded to the creep displacement of the test specimen. The scanning rate employed was

100 scans/sec and the resolution of the system was 0.5 μm . Detailed descriptions of the strain-measurement technique can be found in reference 17. The data acquisition system consisted of a personal computer and an analog chart recorder (Model 6224, Soltec, San Fernando, CA). A preload of about 10 N was applied to the test specimens and maintained until actual testing. Testing was initiated after a thermal equilibration for about 20 min at the test temperature. Six tensile stresses ranging from 10 to 81 MPa were used. One specimen was used at each stress. The gauge-section nominal tensile stress σ was calculated as follows:

$$\sigma = \frac{P_t}{\frac{\pi d^2}{4}} \quad (1)$$

where P_t is the applied tension load (N) and d is the gauge-section diameter (mm) of the tension test specimens. Testing was conducted in accordance with ASTM Test Method C1291 (ref. 19).

Compression Testing

In pure compression testing, cylindrical test specimens 3.5 mm in diameter and 7.5 mm in height (gauge length) were used. Figure 5 shows the test specimen and experimental setup for compression creep testing. As in the tension testing, test specimens with cylindrical cross sections instead of square cross sections were used to avoid any possible stress concentration due to bending by misalignment. Even with cylindrical test specimens, several experimental difficulties caused deviation from a simple, homogeneous uniaxial stress state. Buckling of the specimen can occur if the ratio of specimen height h to diameter d (h/d) is large; barreling due to the friction between the specimen end and support platen can take place if the ratio is low (refs. 20 and 21). An h/d ratio range of 1.5 to 2.5 was suggested to moderate both buckling and barreling effects (ref. 20). Consequently, the nominal dimensions of the

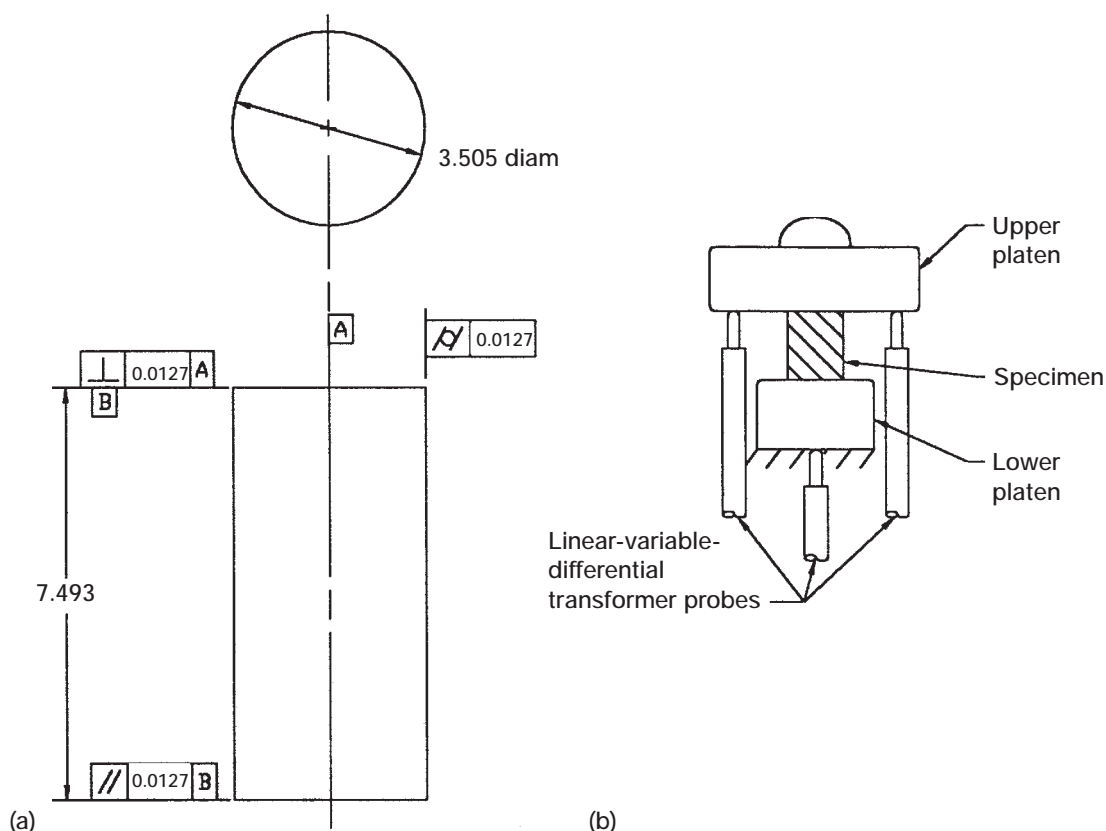


Figure 5.—Pure compression creep testing. All dimensions given in millimeters. (a) Specimen. (b) Test setup.

compression test specimens used in this work (7.5 mm in height and 3.5 mm in diam) were chosen within this recommended range. In addition, a tight tolerance of parallelism (within $\pm 3 \mu\text{m}$) between the two ends of each test specimen was used. It has been reported that for high-strength ceramics, dumbbell-shaped specimens can be used to minimize the indentation of platens by test specimens, thus ensuring more homogeneous stress distribution in the gauge section (ref. 20).

The compression test specimen was mounted between upper and lower Hexoloy SiC platens. The platens in turn were connected to rigid SiC supporters to which the upper and lower push rods were connected. The compression load was applied to the test specimen using an ATS deadweight compression tester. Since creep deformation of ceramic materials is generally significantly smaller in compression than in tension, higher applied stresses ranging from 160 to 630 MPa were used in compression testing. Despite higher applied stresses, no detectable evidence of indentation of the platens by the test specimen was observed from the contact areas after successive creep tests. Five applied stresses (160, 250, 400, 500, and 630 MPa) have been used to date, with one specimen tested at each stress. The gauge-section nominal compressive stress σ was calculated as follows:

$$\sigma = \frac{P_c}{\frac{\pi d^2}{4}} \quad (2)$$

where P_c is the applied compression load (N). The displacement measurements in the gauge section of the test specimen were made by a three-probe, linear-variable-differential transformer (LVDT) with a resolution of $3 \mu\text{m}$. The displacement was monitored and recorded with a Soltec analog chart recorder. The researchers thought that laser extensometry (which is used in the tension creep testing) would yield much better resolution than the LVDT, so it will be used in future compression creep testing.

The influences of specimen geometry and frictional constraint on both stress distribution and creep deformation in compressive creep have been detailed analytically by several investigators. Using a limited finite-element analysis, Birch et al. (ref. 20) found that the creep exhibited by cylindrical compression specimens with an h/d ratio of 1.5 to 2 and by dumbbell-shaped specimens with an h/d ratio of 2.0 was essentially the same. One important assumption made in their analysis was that the specimen ends were completely constrained, thus giving an upper-bound solution. A more detailed analysis by Debschütz et al. (ref. 21), who used cylindrical specimens, identified creep parameters and the various effects of friction and specimen shapes on creep behavior. Friction was known to decrease the strain rate by the factor K , which is the ratio of creep rates for the complete constraint case and the frictionless case. For a typical specimen with an h/d ratio of 2.0, the creep rate deviation ranged from 8 to 14 percent for the values of 1 to 5 of the stress exponent N . Different specimen shapes were also shown to influence the deviation significantly: For an h/d ratio from 0.5 to 2.0, the creep rate deviated from 8 to 35 percent for $N = 1$. Hence, friction at the loaded ends of test specimens has a significant influence on stress distribution and creep behavior and, consequently, on the estimation of creep parameters.

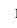
Appropriate lubrication is recommended for room-temperature compression testing of metallic materials, either a TFE-fluorocarbon sheet, molybdenum disulfide, or other materials, according to ASTM Test Method E9 (ref. 22). However, for compression creep testing of advanced ceramics at elevated temperatures, it is questionable whether an appropriate lubricant exists that causes no undesirable effects at the contact area. Some chemical reactions such as corrosion or oxidation at the contact area would result in inhomogeneous stress distribution, probably giving rise to irregular creep deformation and possibly leading to premature specimen failure at the contact area in the form of lateral splitting and/or buckling. Typical examples of specimen configurations used in compression creep testing are summarized in table I.

Uniaxial Flexure Creep Testing

In four-point uniaxial flexure testing, flexure beam specimens were loaded in a SiC four-point flexure fixture with 20-mm inner and 40-mm outer spans using an ATS deadweight creep tester. Test specimens were nominally 3 mm in height, 4 mm in width, and 50 mm in length. The general specifications on the test fixture, test specimens, and temperature control used in uniaxial flexure testing were in accordance with ASTM Test Method C1211 (ref. 28). Each specimen was mounted to the test fixture with a cyanoacrylate adhesive. This adhesive has long been

TABLE I. TYPICAL TEST CONDITIONS AND SPECIMEN CONFIGURATIONS USED IN COMPRESSION
CREEP TESTING

Material	Temperature, °C	Applied stress, MPa	Specimen cross section and height, mm	Reference
Si ₃ N ₄ /Al ₂ O ₃	1200/1000	60,120/86~121	9 ^a by 25.4	Ferber, Jenkins, and Tennery (2)
Si-SiC	1300	130 to 270	3 by 3 by 8	Wiederhorn et al. (1)
3Y-TZP	1100 to 1200	20 to 70	4 by 8	Debschütz et al. (21)
Al ₂ O ₃	1150/1300	220 to 270/35 to 130	6.4 by 12.7	Page et al. (23)
YAG	1400 to 1610	(b)	3 by 3 by 6	Parthasarathy, Mah, and Keller (24)
Si ₃ N ₄ -MgO	1400	175 to 700	3 by 3 by 9	Lange, Davis, and Clarke (25)
RBSN	1270 to 1370	160 to 400	4.25 by 6.4	Birch et al. (20)
			3.2 by 4.8 (dumbbell)	
BeO	650 to 1750	12.5 to 140	2 by 2 by 5	Corman (26)
YSZ	1300 to 1550	50 to 160	2.5 by 2.5 by 5	Fernandez et al. (27)

^a The symbol  represents a cylindrical cross section.

^b Strain rate applied.

used effectively in elevated-temperature testing of various silicon nitrides, aluminas, and silicon carbides without producing any harmful chemical reaction. The fixture assembly with mounted specimen was then placed between two rigid SiC supports connected to the push rods of the creep tester. An initial preload of 10 N was applied to the specimen and maintained until the actual testing. An LVDT probe was placed underneath the center point (tension side) of each test specimen to measure creep deflection. Seven applied loads were used, ranging from 36 to 201 N with corresponding nominal (max) stresses from 29 to 162 MPa. The nominal gauge-section (inside the inner span) maximum tensile stress was calculated assuming an idealized (elastic) condition as follows:

$$\sigma = \frac{3}{2} \frac{P(L_o - L_i)}{bh^2} \quad (3)$$

where P is the applied load (N); L_o and L_i are the outer and inner spans (mm), respectively; and b and h are the width and height (mm) of the flexure test specimen, respectively. The experimental setup for the four-point uniaxial flexure testing and the test specimen geometry are shown in figure 6. The creep deflection of the test specimen was recorded with a Soltec analog chart recorder.

Ball-on-Ring Biaxial Flexure Creep Testing

In ball-on-ring biaxial flexure creep testing, 2-mm-thick, 45-mm-diameter disk specimens were loaded using a ball-on-ring biaxial fixture with an ATS deadweight creep tester. The test fixtures included the upper loading fixture and the lower support fixture, which consisted of a series of SiC support balls and a SiC support block. Nine 9-mm-diameter balls were mounted on the flat support block, evenly spaced peripherally to form a pitch diameter of 40 mm. The upper SiC 9-mm-diameter loading ball was flattened by grinding to form a small rounded surface 1.31 mm in diameter. The disk specimen was placed on the lower fixture with the support balls in place. The flat surface of the upper loading ball was then brought into contact with the center of the test specimens. The specimen-fixture assembly was completed with specially designed alignment tools and the cyanoacrylate adhesive. The center deflection of the test specimens was determined with an LVDT and a Soltec analog chart recorder. Four applied loads were used, ranging from 45 to 182 N with corresponding nominal (max) stresses from 29 to 115 MPa. One test specimen was used at each applied stress. A schematic of the test setup is shown in figure 7. The nominal maximum tensile stress (σ in biaxial stress) of disk specimens occurring within the inner uniformly pressed contact area, assuming an idealized (elastic) condition, was calculated as follows (ref. 29):

$$\sigma = \frac{3P(1+\nu)}{4\pi t^2} \left[1 + 2\ln \frac{a}{b} + \frac{1-\nu}{1+\nu} \left(1 - \frac{b^2}{2a^2} \right) \frac{a^2}{R^2} \right] \quad (4)$$

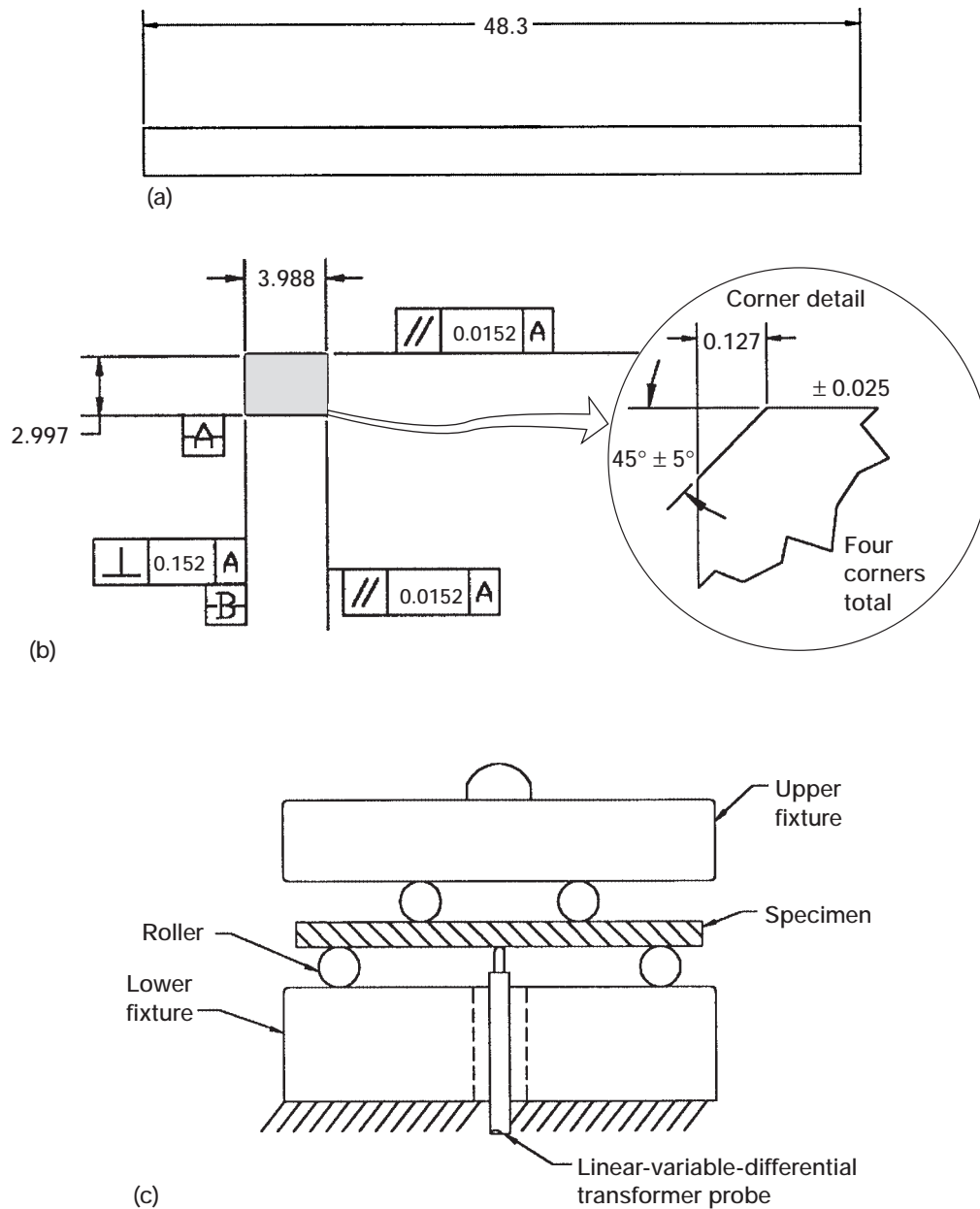


Figure 6.—Four-point uniaxial flexure creep testing. All dimensions given in millimeters.
(a) Specimen, front view. (b) Specimen, side view. (c) Test setup.

where ν is Poisson's ratio; t is the specimen thickness (mm); a and b are the lower support-ring radius and the flat-section radius (mm) of the upper loading ball, respectively; and R is the specimen radius (mm). Equation (4) indicates that the effect of contact radius b on stress is greatest for the second term $2 \ln(a/b)$ and almost negligible for the third term. Therefore, it is important to determine how a change in b affects the resulting stress, since during long-term testing there might be an increase in b that could be attributed to increased plasticity or creep. Figure 8 shows normalized stress ($4\pi t^2 \sigma / [3P(1+\nu)]$) as a function of contact radius b for the given a (20 mm), ν (0.3), and R (22.5 mm). As can be seen in the figure, the effect of b is significant at smaller values of b but is insignificant at around $b \geq 0.6$ mm. For example, the change in b from 0.65 to 0.70 mm results in a decrease in stress of less than 3 percent. Hence, some slight change in b during testing would be unimportant.

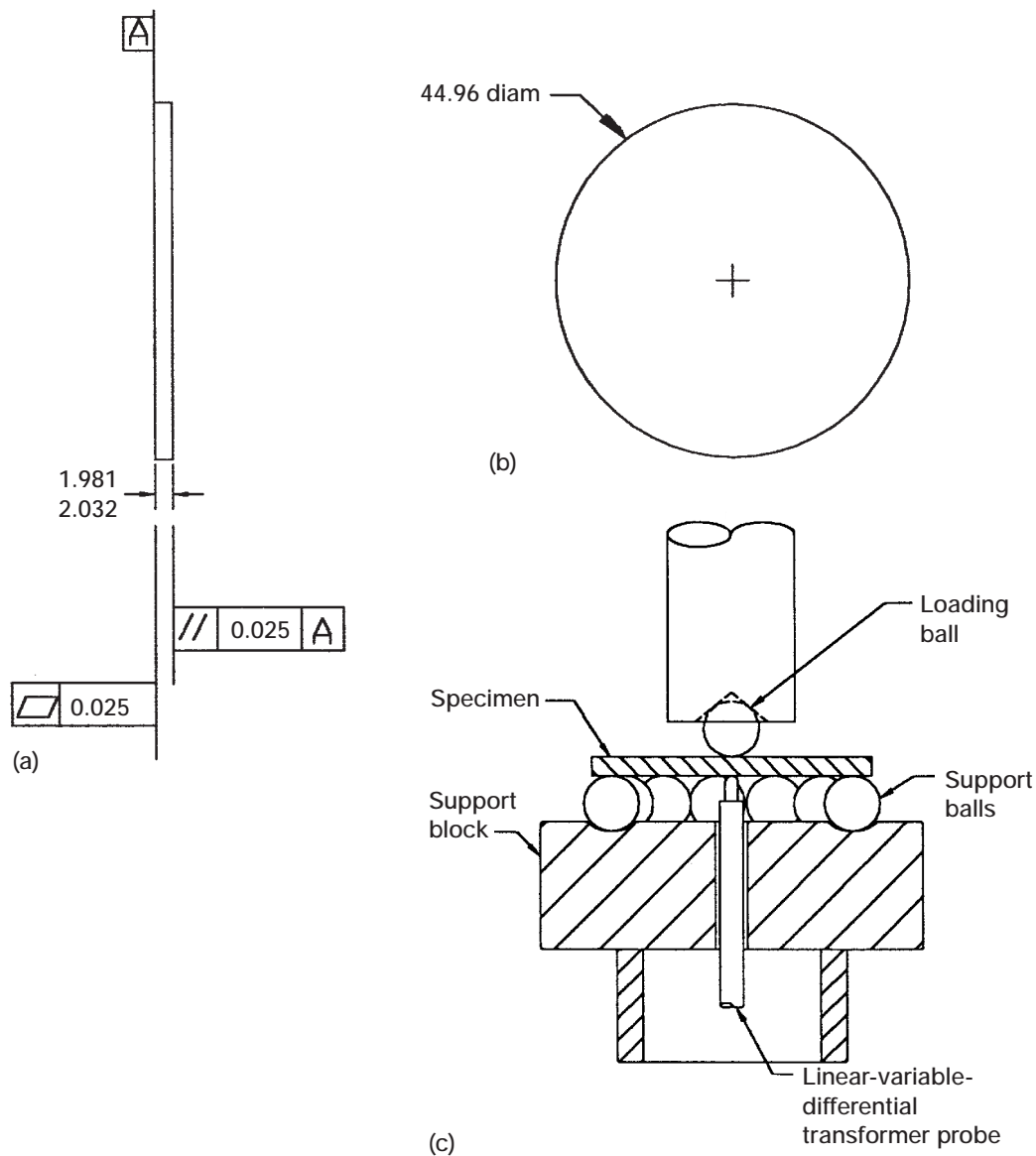


Figure 7.—Ball-on-ring biaxial flexure creep testing. All dimensions given in millimeters.
 (a) Specimen, front view. (b) Specimen, side view. (c) Test setup.

The flat surface of the loading ball appeared to give almost complete contact with the test specimen surface rather than a ring contact, achieving presumably uniform pressure within the contact area. This was attributed to the increased compliance of test specimens as a result of enhanced elevated-temperature creep and plasticity. In ambient-temperature ball-on-ring biaxial testing, a ball without a flat surface can be used to obtain approximately uniform contact pressure (refs. 29 and 30). However, at elevated temperatures, the ball tends to penetrate into or indent the specimen surface, resulting in a nonuniform contact pressure. In fact, such a ball configuration has been used in indentation and/or impression creep testing to characterize the variable creep behavior of materials (refs. 31 and 32). It should be noted that at ambient temperature, the flat ball configuration usually gives a ring contact due to the elastic deformation of the test specimen; thus, a flat ball has been used as an upper loading ring for much room-temperature, ring-on-ring biaxial testing for ceramic materials (ref. 33).

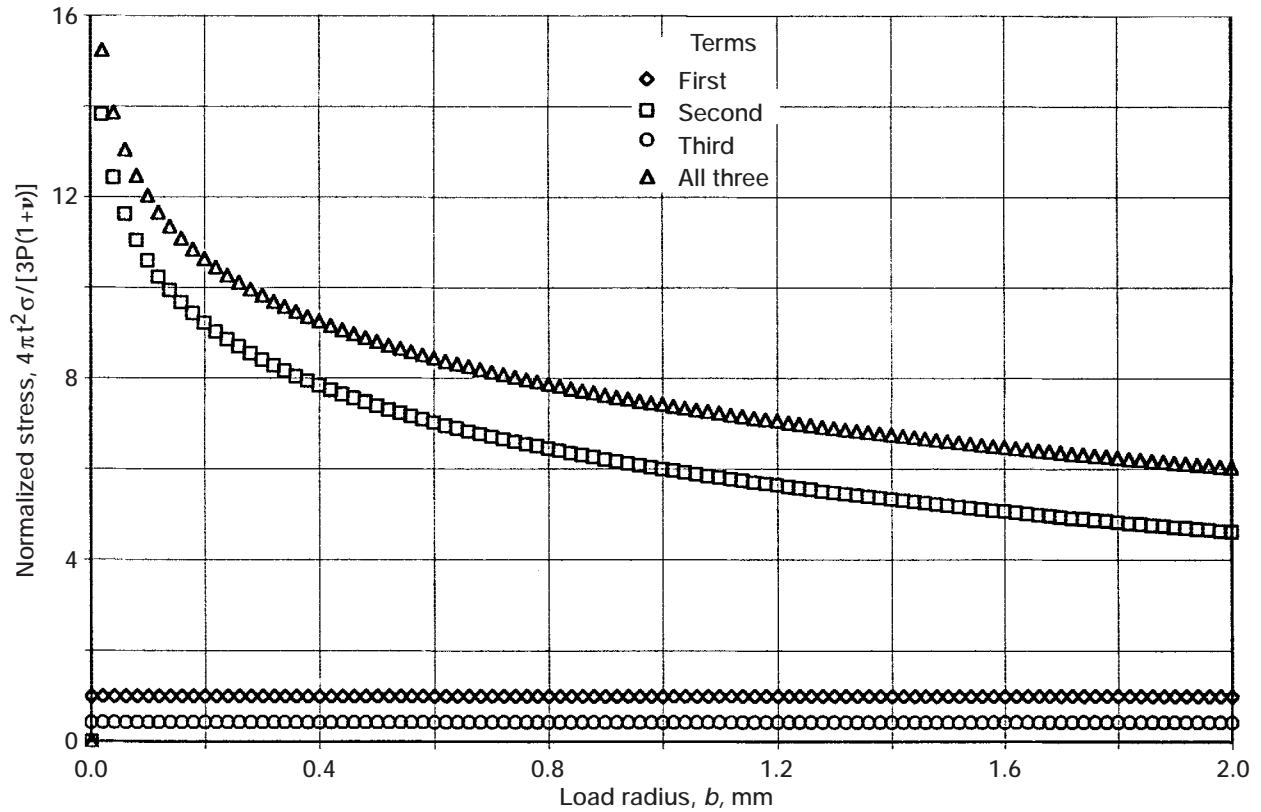


Figure 8.—Normalized stress $4\pi t^2 \sigma / [3P(1+\nu)]$ as function of contact radius b (eq. (4)) in ball-on-ring biaxial flexure.

Ring-on-Ring Biaxial Flexure Creep Testing

In addition to ball-on-ring biaxial flexure testing, other biaxial creep testing was conducted in the ring-on-ring flexure configuration. The biaxial test fixture consisted of upper and lower loading fixtures. The upper loading fixture comprised a loading block and seven evenly spaced 9-mm-diameter SiC loading balls, peripherally forming a pitch diameter of 15 mm. The lower support fixture was the same as that used in the ball-on-ring biaxial flexure testing, that is, a series of SiC balls with a pitch diameter of 40 mm placed on the SiC support block. The resulting loading and support ring diameters were 15 and 40 mm, respectively. The test disk specimens used in the ring-on-ring biaxial testing were the same as those in the ball-on-ring biaxial testing. As in the ball-on-ring biaxial testing, test specimens and fixtures were assembled with specially designed alignment tools and the cyanoacrylate adhesive. The center deflection of each test specimen was determined using an LVDT probe and an analog chart recorder. Test procedures in ring-on-ring biaxial testing were identical to those in ball-on-ring testing. Testing was conducted in an ATS deadweight creep test frame. Four applied loads were used, ranging from 200 to 565 N with corresponding nominal (max) stresses ranging from 29 to 81 MPa. The nominal maximum tensile stress (biaxial stress σ) of disk specimens within the loading ring, assuming an idealized (elastic) condition, was calculated as follows (ref. 29):

$$\sigma = \frac{3P}{4\pi t^2} \left[2(1+\nu) \ln \frac{a}{b} + \frac{(1-\nu)(a^2 - b^2)}{R^2} \right] \quad (5)$$

where b is the upper loading-ring radius.

One test specimen was used at each applied stress. A schematic of the ring-on-ring biaxial flexure experimental setup is shown in figure 9. Ring-on-ring biaxial testing at elevated temperatures was used to determine stress-rupture (ref. 34) and slow crack growth (dynamic fatigue) (ref. 35) behaviors of silicon nitrides.

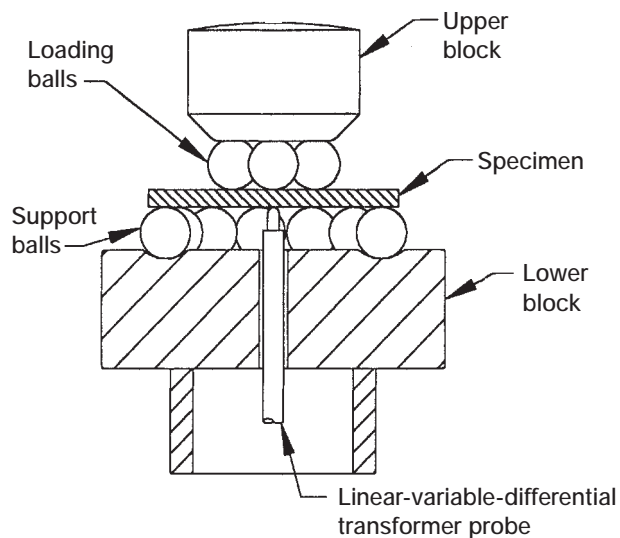


Figure 9.—Test setup in ring-on-ring biaxial flexure creep testing.

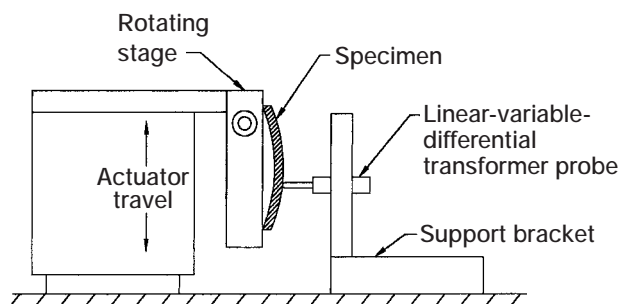


Figure 10.—Test setup for profile measurements of crept specimens.

A different lower support block with a ball race ground (with the same pitch diameter of 40 mm) similar to a typical thrust-ball-bearing race was used at first, primarily to position the loading balls more easily and accurately. However, in load-displacement diagrams the fixture showed some degree of hysteresis, which was indicative of a frictional constraint occurring between the race and the support balls. The lower support block was then modified to have only a flat surface instead of a ball race. This modification caused the load-displacement diagram to be much more linear, thus minimizing frictional constraint. The frictional constraint observed in the ball race biaxial fixture appeared to be very similar to that occurring with uniaxial four-point flexure when loading pins are fixed or placed on V-grooves (refs. 36 and 37).

Measurements of Deflection Profiles of Crept Specimens

Deflection profiles of some tested specimens that were crept in uniaxial and biaxial flexure were measured. Profiles were determined by tracing over the convex surfaces of crept specimens with an LVDT probe. The apparatus used for the profile measurements is shown in figure 10. The crept specimen was mounted with two-sided tape on a base, which was attached to the actuator of an electromechanical test frame (Model 8562, Instron, Canton, MA). The LVDT was attached to a stationary test-frame table. As the actuator moved up and down, the specimen moved accordingly, its tension surface remaining in contact with the spring-loaded LVDT probe. A full specimen

profile was produced by recording the actuator position signal to give the specimen position and the LVDT signal to give the specimen deflection.

The deflection profiles of each disk specimen crept in ring-on-ring flexure were determined along the diameter in the three directions of 0° (base reference), 45°, and 90°. The profiles of uniaxial-flexure-crept specimens were measured along the longitudinal direction. In the future, data on the deflection profiles will be compared with predictions made by the CARES/Creep program. The deflection profiles could be used to verify the design program because CARES/Creep should be able to provide the corresponding specimen creep deformation and stress distributions at any time.

EXPERIMENTAL RESULTS

Tension Creep Testing

A summary of tensile creep displacements as a function of time at five applied stresses at 1300 °C is presented in figure 11. Since no specimen failed before the test interruption, the end point of each curve corresponds to the end of the test. Test times spanned from about 20 days at 81 MPa to about 60 days at 41 MPa. Surfaces of the tested specimens revealed some degree of oxidation, depending on the test time period. However, no visible signs of the microcracks associated with enhanced creep were observed on the specimens, even after the removal of their oxide layers. The displacement curves for the specimens tested at 10 and 28 MPa seemed to show steady-state creep regions where the displacement rate remained relatively constant. By contrast, the curves for specimens tested at 57 and 81 MPa showed no well-defined steady-state region, but rather a change in displacement rates with time. As a result, no distinct region of primary creep was observed for these specimens. The absence of a secondary steady-state creep region will be addressed in more detail in the Discussion section.

Compression Creep Testing

The results of the compression creep testing are shown in figure 12, where compressive creep displacements are plotted as a function of time for five applied stresses. Note that for the same order of magnitude of creep displacement, the applied stresses in compression were significantly greater than those in tension. This shows how creep displacement of NC132 silicon nitride is considerably greater in tension than in compression at the same (absolute)

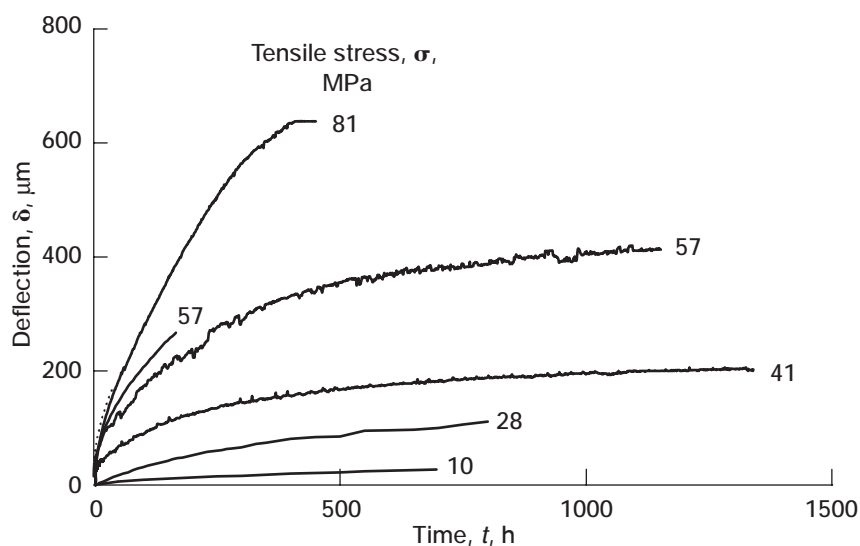


Figure 11.—Tensile creep displacement as function of time determined at five nominal tensile stresses for NC132 silicon nitride at 1300 °C.

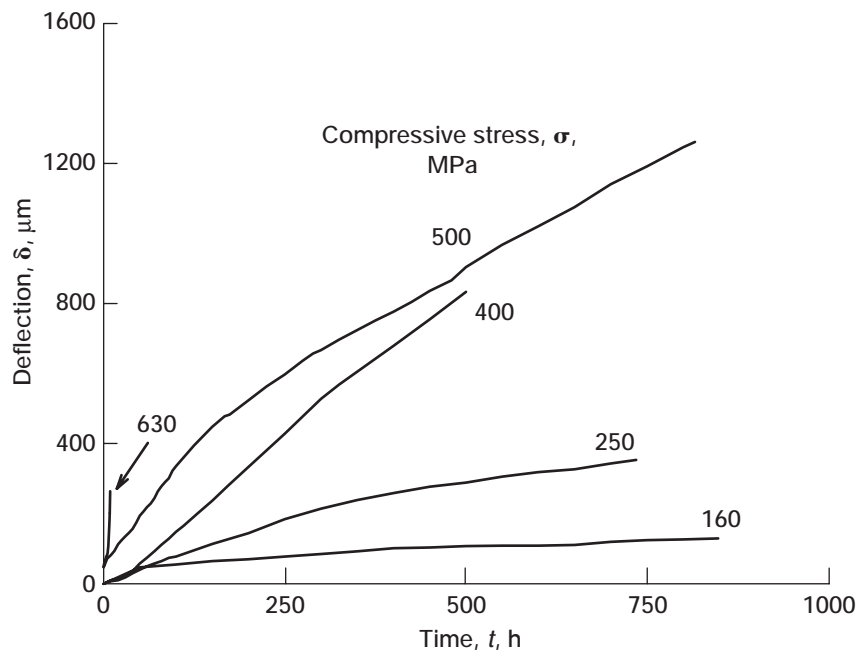


Figure 12.—Compression creep displacement as function of time determined at five nominal compressive stresses for NC132 silicon nitride at 1300 °C.

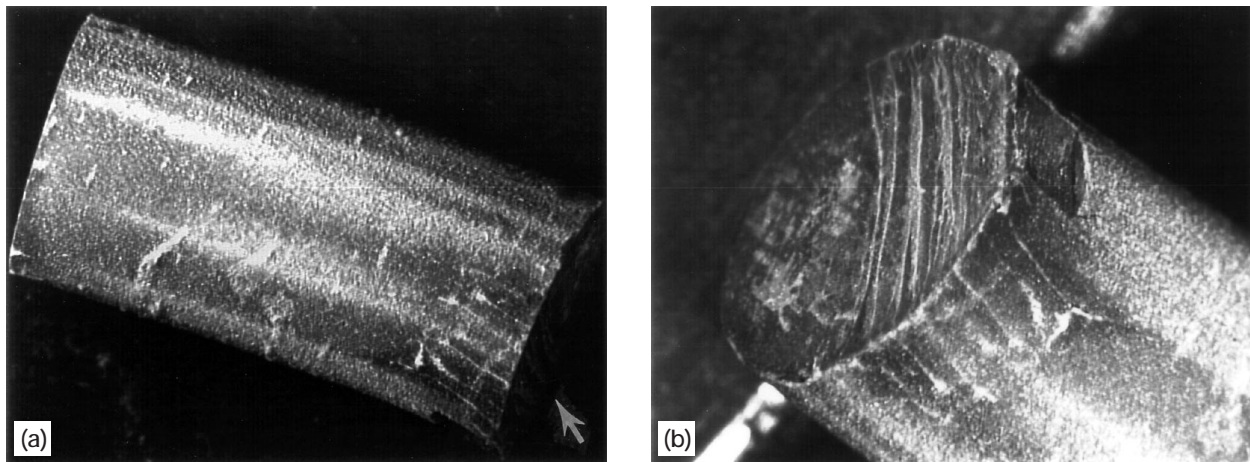


Figure 13.—Inhomogeneous creep deformation along specimen length occurring in compression creep testing of NC132 silicon nitride at 1300 °C. Nominal compressive stress applied, 400 MPa; test time, 800 h. (a) Overall. (b) Enlarged and viewed from arrow direction marked in (a).

applied stress. It should be noted again that the relatively low-resolution LVDT probe was employed in the compression creep testing (instead of the laser extensometry used in the tension creep testing). As a result, the use of high-compression stresses was unavoidable to achieve a reasonably accurate monitoring of compression creep displacement.

At the highest compressive stress of 630 MPa, the specimen failed in a similar manner to fast fracture, leaving many tiny fragments. The data for this specimen were not used in the analysis. The specimen tested at 400 MPa revealed nonuniform longitudinal creep deformation, with some planner cracks originating from one end of the test specimen, as shown in figure 13. This could be attributed to load misalignment (bending induced), material inhomogeneity, and/or frictional constraint at the loaded end. Lateral tensile stresses would cause this kind of lateral splitting. The corresponding displacement curve showed no clear evidence of lateral tensile stresses, although a slight kink in the curve was detected around 300 h. It was observed that a sudden increase of creep deflection (which was

probably associated with the lateral splitting) took place close to the time of test interruption. Hence, the creep displacements determined at 400 MPa were included in the data analysis. As seen in figure 12, most of the curves (except the one at 500 MPa) exhibited the steady-state creep region, which is in somewhat good contrast with the tensile creep curves. However, no distinct primary region was observed for most of the test specimens. The undesirable barreling deformation did not occur for any of the test specimens, indicating a good agreement with the previous studies by Birch et al. (ref. 20) and Debschütz et al. (ref. 21), where the barreling effect was minimized with the use of specimen h/d ratios from 1.5 to 2.5. Note that the ratio used in this study was 2.1.

Uniaxial Flexure Creep Testing

A summary of creep displacements (deflections) as a function of time in four-point uniaxial flexure is presented in figure 14. The figure shows the maximum nominal stresses from 29 to 162 MPa. The end point of each curve represents the time of interruption. In spite of appreciable creep deflection, no specimen failed before the interruption of the testing period, which ranged from 17 days for the highest stress of 162 MPa to about 100 days for the lowest stress of 29 MPa. Regardless of the nominal applied stresses, creep rate changed with time, so that no definite steady-state creep region could be determined. Since no explicit secondary steady-state creep region existed, a clear-cut transition between the primary and secondary regions was also not definable.

Figure 15 shows the typical difference in appearance between the tension and compression sides of a crept sample viewed with optical microscopy. The specimen was subjected to 57 MPa for about 1600 h, after which voids and/or damage between the tension and compression sides were apparent. It was observed optically that voids and/or microcracks were significant on the tension side for many advanced ceramics, whereas on the compression side, no damage and/or voids were evident (ref. 38), showing a definite difference in creep behavior between tension and compression. A neutral-axis shift toward the compression side is inevitable to reach an equilibrium condition for a new composite beam, combined with a less dense tension side and an original dense compression side. In some cases, optical microscopy might not be sufficient to reveal the detailed features of such damages. A high-resolution microscopy such as scanning electron microscopy (SEM) or preferably transmission electron microscopy (TEM) should be employed for those cases.

Figure 16 shows the deflection profiles of the crept flexure beam specimens subjected to applied stresses of 29 and 41 MPa at interruption times of 2000 and 170 h, respectively. The profiles were measured as described in Experimental Procedures. As noted from the figure, regardless of applied stress and interruption time, each deflection profile was symmetrical with respect to the center of the flexure beam specimen. Also, the technique used in this study was better than the optical technique used in the previous studies where the specimen profile was determined using a low-power optical microscope (refs. 38 and 39).

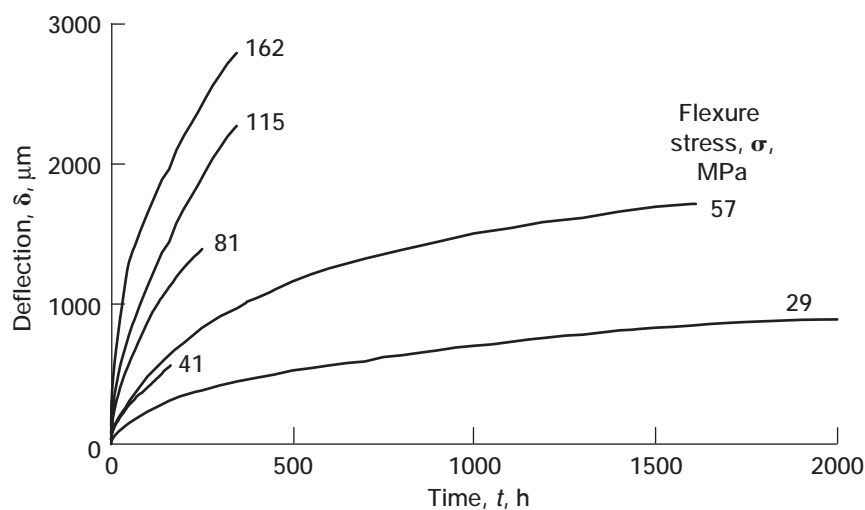


Figure 14.—Four-point uniaxial flexure creep displacement as a function of time determined at different nominal stresses for NC132 silicon nitride at 1300 °C.

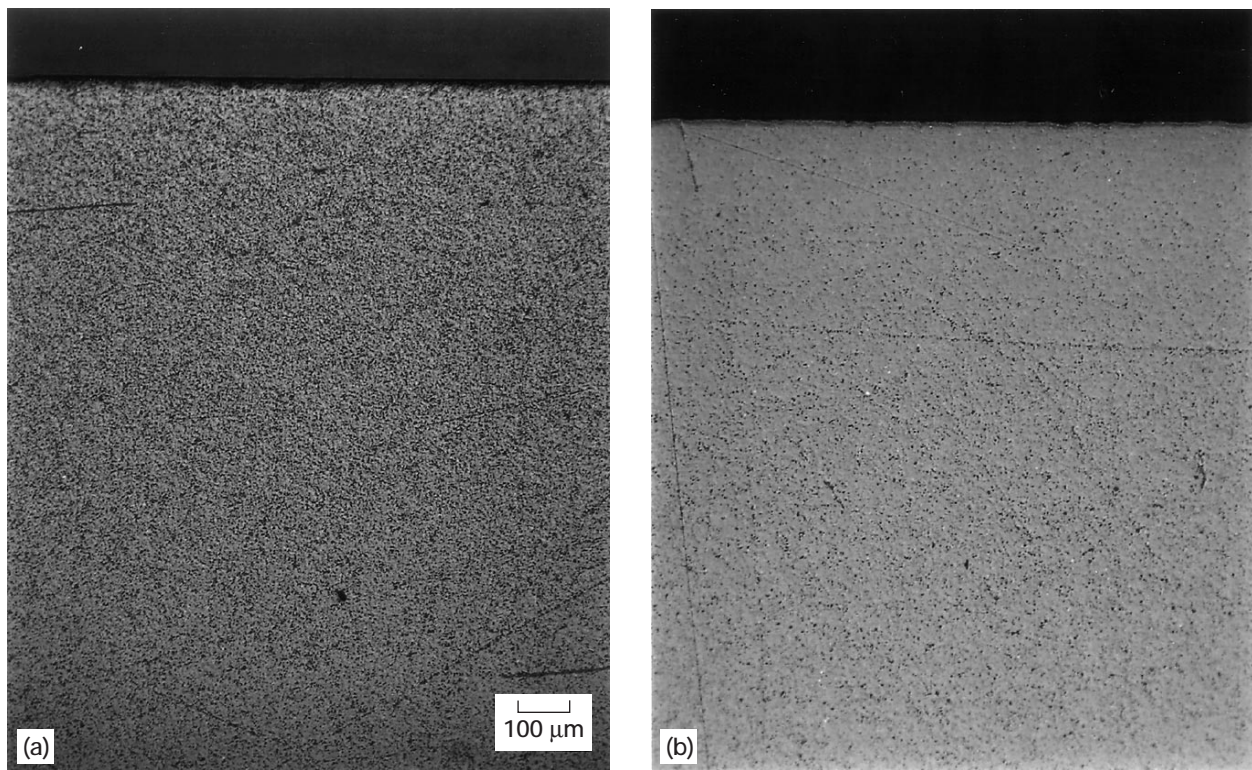


Figure 15.—Difference in appearance between tension and compression sides of four-point flexure beam specimen of NC132 silicon nitride tested for 1600 h at 57 MPa and 1300 °C. (a) Tension side. (b) Compression side.

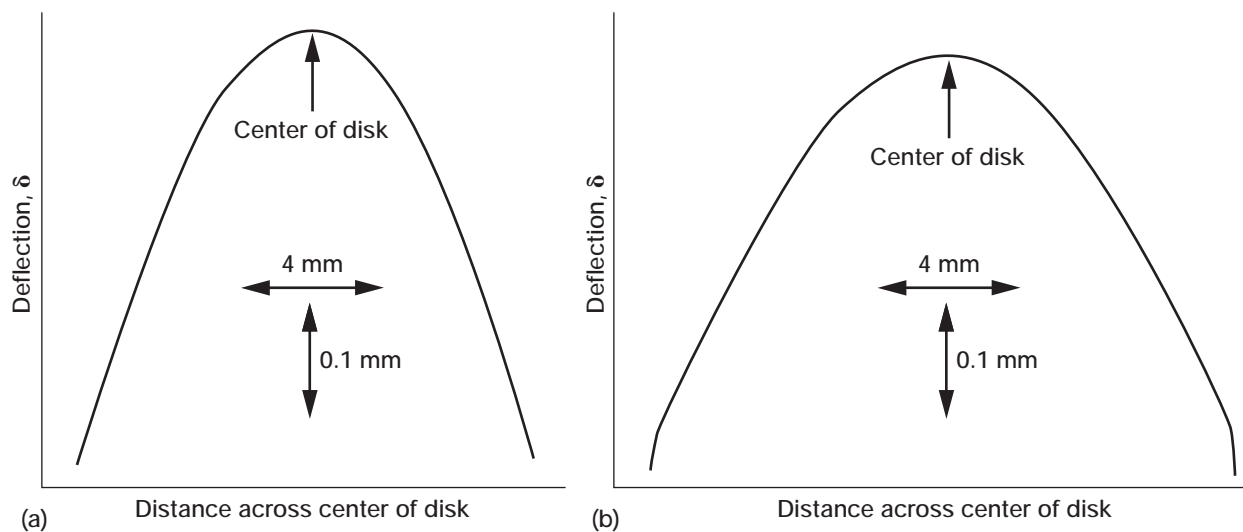


Figure 16.—Deflection profiles along specimen length for four-point flexure crept specimens of NC132 silicon nitride tested at 1300 °C. (a) Nominal stress, 29 MPa; test time, 2000 h. (b) Nominal stress, 41 MPa; test time, 170 h.

Ball-on-Ring Biaxial Flexure Creep Testing

Figure 17 presents a summary of creep displacements as a function of time determined at different nominal stresses in ball-on-ring biaxial flexure creep testing. Again, the end point of each curve represents the time of test interruption. As in the tension, uniaxial flexure, and ball-on-ring (and ring-on-ring) biaxial flexure testing, no test (disk) specimen failed before the end of the testing period, which ranged from about 20 days for the highest stress of 81 MPa to about 100 days for the applied stress of 41 MPa. At the lower stresses of 41 and 29 MPa, the primary creep region seemed to be accompanied by a secondary steady-state creep region. However, it is not yet clear whether the primary or secondary creep regions exist in the curves for the higher applied stresses of 57 and 81 MPa. Irrespective of applied stress and test time, no visible damages or microcracks developed at the region of the maximum tensile stress, that is, beneath the inner loading contact area. Observation of the crept specimens supported the conclusion that the loading ball was in nearly full contact rather than in ring contact with the test specimen surfaces, which was attributed to the increased plasticity and creep of the specimens during the tests. Hence, it is believed that the use of a stress formula (eq. (4)) based on the assumption of full contact is justified. The typical appearance of the contact area on the surface of a crept disk specimen showing full contact is presented in figure 18.

Ring-on-Ring Biaxial Flexure Creep Testing

A summary of creep deflection as a function of time determined at different nominal stresses in ring-on-ring biaxial flexure creep testing is shown in figure 19. As in tension, uniaxial, and ball-on-ring biaxial flexure testing, no specimen rupture occurred before test interruption. The testing period ranged from 10 to 12 days for the lower applied stresses (≤ 57 MPa for about 45 days for a high stress of 81 MPa). Considering the relatively short test times, it would be premature to draw any conclusion regarding the creep curves obtained from stresses ≤ 58 MPa. For the disk specimen tested at the highest stress of 81 MPa, the displacement rate changed with time, making it difficult to define the primary and secondary steady-state regions. Some localized damages in the form of micro- and macrocracks were observed in this disk specimen, but only beneath the upper loading balls, as shown in figure 20. A previous study (S.R. Choi, 1997, NASA Glenn Research Center, Cleveland, OH, Elevated Temperature Slow Crack Growth Testing of a Silicon Nitride in Uniaxial and Biaxial Flexure Loading Conditions, unpublished) using both analytical and experimental approaches showed that a uniform biaxial tensile stress occurred within the loading ring in accordance with equation (5) and that a maximum localized tensile stress occurred beneath the loading balls also

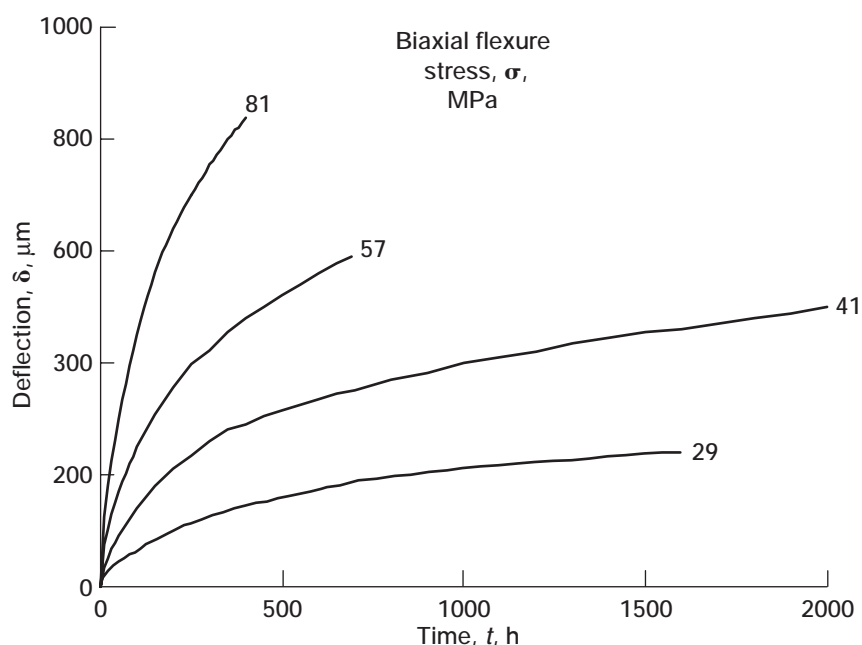


Figure 17.—Ball-on-ring biaxial flexure creep displacement as function of time determined at different nominal stresses for NC132 silicon nitride at 1300 °C.

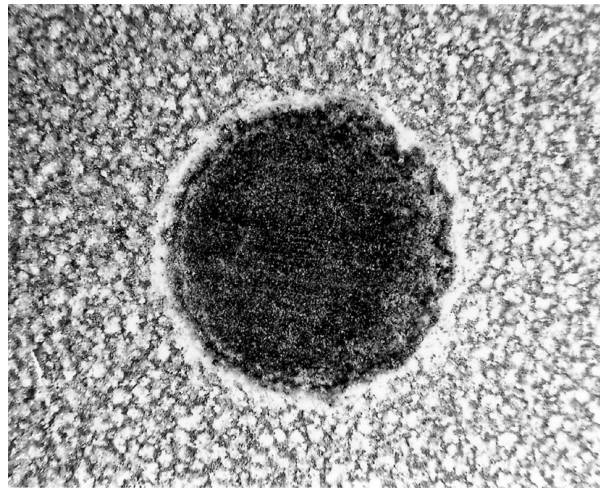


Figure 18.—Appearance of contact area in crept disk specimen showing full contact in ball-on-ring biaxial flexure creep testing of NC132 silicon nitride at 1300 °C. Nominal applied stress, 58 MPa; test time, 300 h.

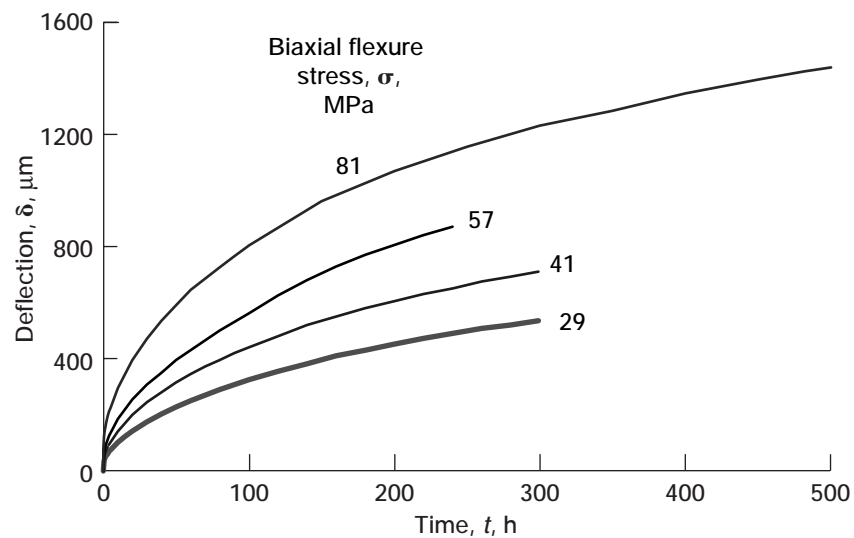


Figure 19.—Ring-on-ring biaxial flexure creep displacement as function of time determined at four nominal stresses for NC132 silicon nitride at 1300 °C.

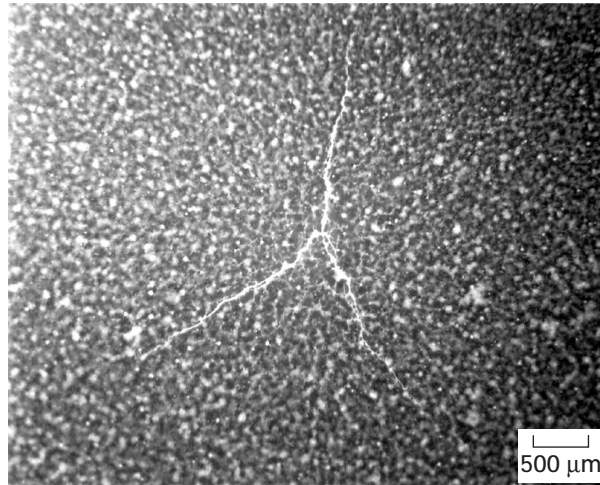


Figure 20.—Cracks directly beneath loading ball of crept disk specimen in ball-on-ring biaxial flexure creep testing. Specimen subjected to nominal applied stress of 81 MPa for 1000 h at 1300 °C.

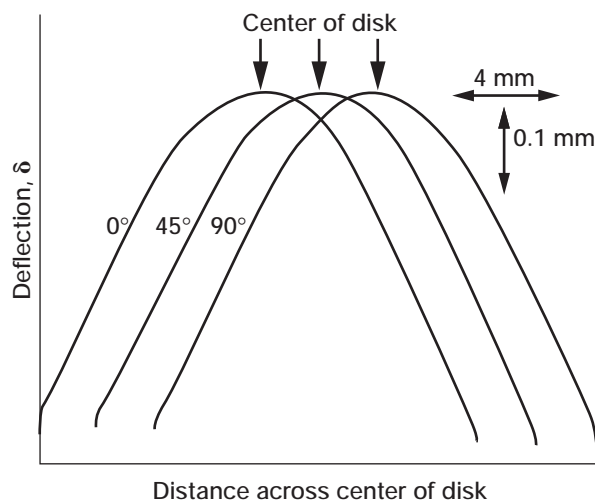


Figure 21.—Deflection profiles across diameter of ring-on-ring biaxial flexure (crept) disk specimen. Specimen subjected to nominal applied stress of 81 MPa for 1000 h at 1300 °C. Profiles determined in three directions 45° apart.

in this case, which caused micro- and macrocracks in this area. This localized stress would not have a significant effect on the creep behavior of relatively large disk specimens because the overall stress distributions governing creep displacement would remain unchanged. Specimens tested at stresses lower than 81 MPa showed no sign of damage, either in the maximum localized stressed region or in the biaxially stressed region (i.e., within the loading ring).

Figure 21 shows deflection profiles determined from a crept disk specimen that was subjected to 81 MPa for 1000 h at 1300 °C. Three profiles representing 0°, 45°, and 90° were measured diametrically as described in Experimental Procedures. The 0° profile represents the angle passing beneath the loading ball, which was taken as the reference base angle. As can be seen in the figure, the profiles of the specimen deflection were all consistent, with good continuity and symmetry. This confirms that the maximum localized tensile stress occurring beneath the loading balls had no significant effect on the overall creep deformation of the disk specimen. If the maximum localized stress had caused an apparent localized deformation, there would have been some discontinuity in the profile around the stressed region.

DISCUSSION

Determinations of Nominal Creep Strain

In this section, appropriate relations to convert creep displacement to creep strain will be presented for each specimen-loading configuration.

Pure tensile and pure compressive creep.—In pure tensile or pure compressive creep, the strain can be determined as follows:

$$\varepsilon = \left| \frac{\Delta l}{l_o} \right| \quad (6)$$

where ε is the nominal strain (not true strain), Δl is the elongation (in tension) or contraction (in compression), and l_o is the gauge length. The gauge length in tensile creep can be defined (set) from any distance between the two flags in conjunction with the laser extensometry system; the gauge length in compressive creep corresponds to the specimen height.

Four-point uniaxial flexure creep.—The strain in four-point uniaxial flexure creep can be estimated using the following idealized (elastic) beam theory:

$$\varepsilon = \left[\frac{12h}{(3L_o^2 - 4a^2)} \right] \delta \quad (7)$$

where $a = (L_o - L_i)/2$ and δ is the center deflection of the test specimens.

Ball-on-ring biaxial flexure creep.—Kirstein and Woolley (ref. 40) have developed an expression for the center deflection of a disk specimen in ball-on-ring biaxial flexure. The polynomial approximation to the exact solution is given by

$$\delta = \left\{ -0.0642 + 0.5687(1 - \nu) + \left[-0.3793 + (1 - \nu^2) \frac{a^2}{R^2} \right] \right\} \frac{Pa^2}{Et^3} \quad (8)$$

where E is Young's modulus and other parameters are as defined in equation (4). The elastic strain and stress relation in the biaxial condition are expressed as

$$\varepsilon_r = \varepsilon_\theta = \varepsilon = \frac{\sigma(1 - \nu)}{E} \quad (9)$$

where ε_r and ε_θ are the radial and hoop strains in the loading area and have a maximum value equal to ε . The corresponding maximum radial or hoop stress σ was given by equation (4). Using equations (4), (8), and (9), the strain as a function of the center deflection δ can be derived as follows:

$$\varepsilon = \left[\frac{3(1 - \nu^2)t}{4\pi a^2} \frac{\beta}{\alpha} \right] \delta \quad (10)$$

where

$$\beta = 1 + 2 \ln \frac{a}{b} + \frac{1 - \nu}{1 + \nu} \left(1 - \frac{b^2}{2a^2} \right) \frac{a^2}{R^2}$$

$$\alpha = -0.0642 + 0.5687(1 - \nu^2) + \left[-0.3793 + (1 - \nu^2) \right] \frac{a^2}{R^2}$$

Ring-on-ring biaxial flexure configuration.—The center deflection of a disk specimen subjected to ring-on-ring biaxial flexure with small deflection is given based on the conventional plate theory of Timoshenko and Woinowsky-Krieger (ref. 40):

$$\delta = \frac{3P(1-\nu^2)}{2\pi t^3 E} \left[b^2 \ln \frac{b}{a} + (a^2 - b^2) \frac{3+\nu}{2(1-\nu)} \right] \quad (11)$$

The above equation is valid when a test specimen diameter is at least 10 times greater than its thickness and when the specimen thickness-to-deflection ratio is greater than 2, that is, for small deflection (ref. 42). For large deflection, when the specimen thickness-to-deflection ratio is less than 1, the state of stresses within the loading ring is no longer in a uniform biaxial condition. This deviation from the biaxial condition is also amplified when the ratio of the loading ring diameter to the supporting ring diameter is increased. A detailed analysis of stress in terms of specimen deflection and geometry can be found in Kao, Perrone, and Capps (ref. 43). To meet the above conditions, the maximum creep deflection was kept smaller than 50 percent of the specimen thickness (2 mm) in all biaxial creep testing.

Using equations (5), (9), and (11), the strain inside the loading ring, which is both in biaxial and maximum, can be derived as a function of center deflection δ as follows:

$$\epsilon = \left[\frac{t}{2(1+\nu)} \frac{B}{A} \right] \delta \quad (12)$$

where

$$B = 2(1+\nu) \ln \frac{a}{b} + (1-\nu) \left(1 - \frac{b^2}{a^2} \right) \frac{a^2}{R^2}$$

$$A = b^2 \ln \frac{b}{a} + (a^2 - b^2) \frac{3+\nu}{2(1-\nu)}$$

The creep strain equations presented above for uniaxial flexure (eq. (7)), ball-on-ring biaxial flexure (eq. (10)), and ring-on-ring biaxial flexure (eq. (12)) were all based on idealized (elasticity) solutions. Therefore, if significant creep, plasticity, relaxation, and/or a possible shift of neutral axis toward the compression side are present, the application of these equations to flexure loading may not be appropriate. Such data should be used with caution when interpreted in terms of strain rate, creep and rupture parameters, and other factors. The same caution should be exercised when stresses in flexure are to be calculated under creep conditions. For simplicity, however, this study used flexure strain and stress (termed “nominal” strain and stress) calculated on the basis of the above idealized solutions.

Nominal Creep-Strain Curves

Figure 22 shows nominal creep strain as a function of time for the five specimen-loading configurations, converted from the creep displacement data using equations (6), (7), (10), and (12). As already seen in the creep displacement data (figs. 11, 12, 14, 17, and 19), except for compressive creep, a well-defined secondary steady-state condition was rarely observed; therefore, no clear demarcation between the primary and secondary creep regions could be defined. For a given nominal applied stress, both magnitude and rate of nominal creep strain depended on loading conditions. A typical example is shown in figure 23, where nominal creep strain was plotted as a function of time for different loading configurations but with the same nominal applied stress of 57 MPa. The overall creep strain and its rate were highest for tension loading, intermediate for uniaxial flexure loading, and lowest for biaxial flexure (ball-on-ring and ring-on-ring) loading. The degree of constraint (due to different stress states) in flexure was increased from uniaxial flexure to biaxial flexure. The results of figure 23 also indicate a significant difference in creep between tension and compression loading. If this difference were not noticeable, creep strain in uniaxial flexure would be similar in magnitude and rate to that in tension.

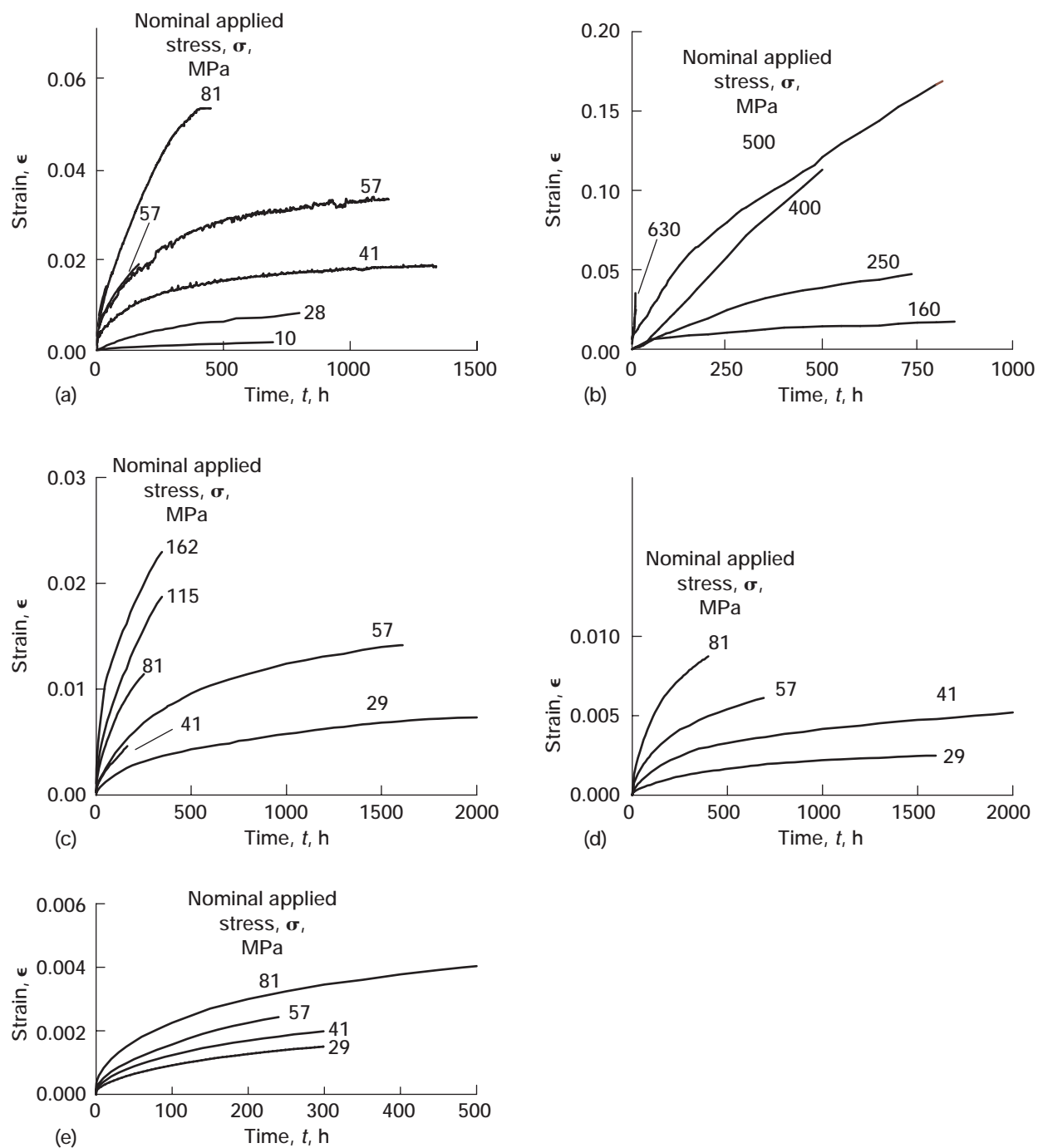


Figure 22.—Nominal creep strain as function of time determined for five specimen-loading configurations for NC132 silicon nitride at 1300 °C. (a) Pure tension. (b) Pure compression. (c) Four-point uniaxial flexure. (d) Ball-on-ring biaxial flexure. (e) Ring-on-ring biaxial flexure.

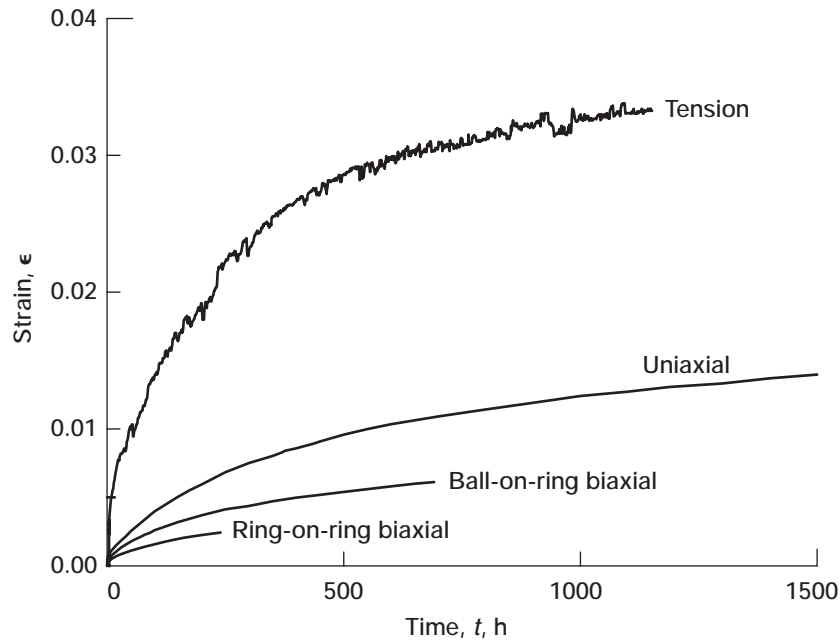


Figure 23.—Comparison of nominal creep strain as function of time determined at four specimen-loading configurations for NC132 silicon nitride at 57 MPa and 1300 °C.

TABLE II. TYPICAL BEST-FIT FUNCTIONS $f(t)$ TO REPRESENT NOMINAL CREEP STRAIN CURVES DETERMINED IN UNIAXIAL FLEXURE LOADING

Nominal applied stress, σ , MPa	Fitted function, ^a $f(t)$	Regression constants		Correlation coefficient, r^2_{coef}
		a	b	
29	$f(t) = at^b$ (power)	3.284×10^{-4}	0.4101	0.9918
57	$f(t) = t/(a + bt)$ (hyperbola)	2.223×10^{-4}	58.150	.9944
81	$f(t) = at^b$ (power)	5.780×10^{-4}	.5437	.9987
115	$f(t) = at^b$ (power)	7.705×10^{-4}	.5450	.9981
162	$f(t) = at^b$ (power)	1.998×10^{-3}	.4170	.9977

^a $f(t)$ is in hours and millimeter per millimeter for strain.

Since, in general, there was no explicit steady-state region, the actual strain rate as a function of time was determined by using a best-fit curve and then taking the derivative of the curve with respect to time as follows:

$$\dot{\epsilon} = \frac{d\epsilon}{dt} = \frac{d}{dt} f(t) \quad (13)$$

where $f(t)$ is a best-fit curve to the creep strain data for each loading condition. Depending on the loading condition and the magnitude of the applied stress, both the power function ($f(t) = at^b$) and the hyperbola function ($f(t) = t/(a + bt)$) resulted in a very reasonable fit to the data with an overall coefficient of correlation r_{coef} greater than 0.99. Figure 24 compares typical functional-fit data to nominal creep strain data in uniaxial flexure. The corresponding fitted functions $f(t)$ to individual nominal applied stresses are also shown in table II. Note that the square of the coefficient of correlation r^2_{coef} for each curve was greater than 0.99, which is indicative of an excellent curve fitting.

Once the function $f(t)$ is known, the strain rate as a function of time can be easily determined using equation (13). A summary of the strain rates determined for all five loading conditions is shown in figure 25. The strain rates range from 10^{-10} to $10^{-8} s^{-1}$, which is typical for most advanced ceramics. As seen in the figure, except for compression loading, the strain rate decreased with increasing time. The degree of decrease in the strain rate was dependent

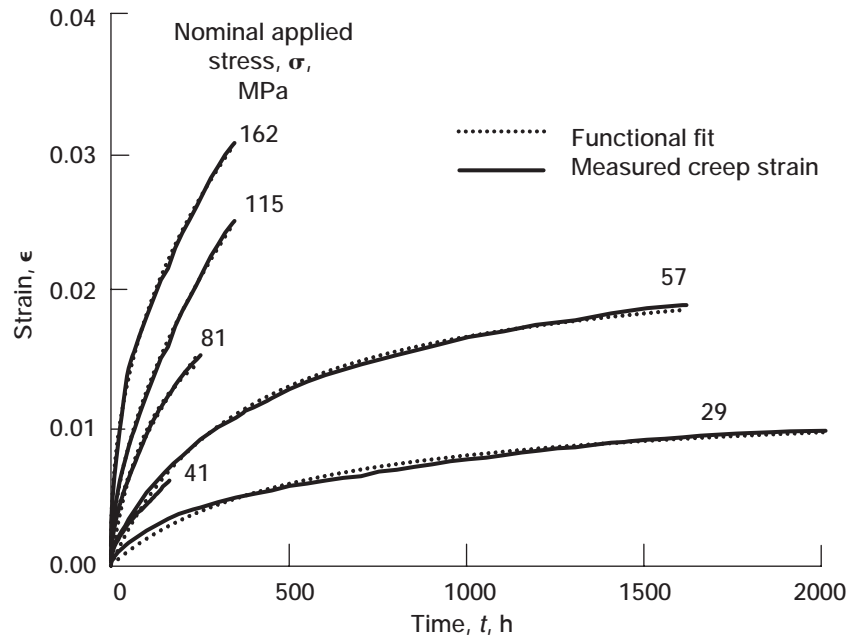


Figure 24.—Comparison of typical best functional-fit data to nominal creep strain data determined in four-point uniaxial flexure creep testing for NC132 silicon nitride at 1300 °C. The corresponding best-fit equations are listed in table III.

on both the applied stress and type of loading. Strictly speaking, no secondary steady-state region existed because the corresponding strain rate was not constant beyond the primary creep region. Therefore, it was not simple to choose a strain rate to represent the so-called steady-state strain rate.

Although many advanced ceramics exhibit a well-defined secondary creep region, many silicon nitrides show no definite steady state. The overall shape of the creep strain curves also varies significantly in different studies. In most materials, a monotonic decrease in strain rate has been observed, even after several thousand hours (ref. 44). A rapid decrease in strain rate from the earliest observations ($<10^{-4}$ strain) is termed “exhaustion creep” (ref. 45). One possible mechanism for decreases in the strain rate during creep for these glass-bonded ceramics (silicon nitrides) may be the redistribution of the grain-boundary amorphous phase, that is, rearrangement of the amorphous film by viscous flow during creep. It has been observed that the glass-phase is redistributed with time such that some boundaries become thicker while others become thinner, leading to increased creep resistance or decrease in the creep strain rate. The hardening effect, the phenomenon of strain rate decrease with time or enhancement of creep resistance, is also affected by grain contact during deformation. It has been postulated that hardening is due to the progressive devitrification that occurs in the residual glassy phase. Detailed descriptions of the mechanisms responsible for the decreasing strain rate at the phenomenological level can be found elsewhere (ref. 45). In general, when creep strain curves exhibit neither steady-state nor tertiary regions, the minimum creep rate at the end of the extensive primary creep is often used synonymously as the steady-state rate.

As mentioned above, except for the case of compression loading, no definite steady state existed, as seen in figure 25. However, the decrease in strain rate was not significant (even after 1500 to 2000 h) compared with cases in the literature in which the decrease in creep strain rate for some silicon nitrides amounted to about 2 orders of magnitude (ref. 45). A decrease in the strain rate of about 1 order of magnitude was observed for cases of tension and uniaxial flexure at 57 MPa. Otherwise, the decrease was generally less than 1 order of magnitude. Hence, for the purpose of analysis, a steady-state creep rate for a given curve was taken by averaging the creep strain rates at two times: at the start of testing from 50 to 400 h and at the end of testing from 220 to 2000 h. The choice of the start time, which was assumed to represent the initiation of the steady-state region, depended on the loading condition and applied stress. A summary of steady-state strain rates thus determined is shown in table III, where strain rates at the start t_s and at the end t_e of testing are listed together with the average strain rate $\dot{\epsilon}_{av}$. Strain rates at t_s and t_e were determined from the corresponding strain-rate equations, shown in figure 25. The average strain rate $\dot{\epsilon}_{av}$ was obtained by averaging the two strains at the start and at the end of testing.

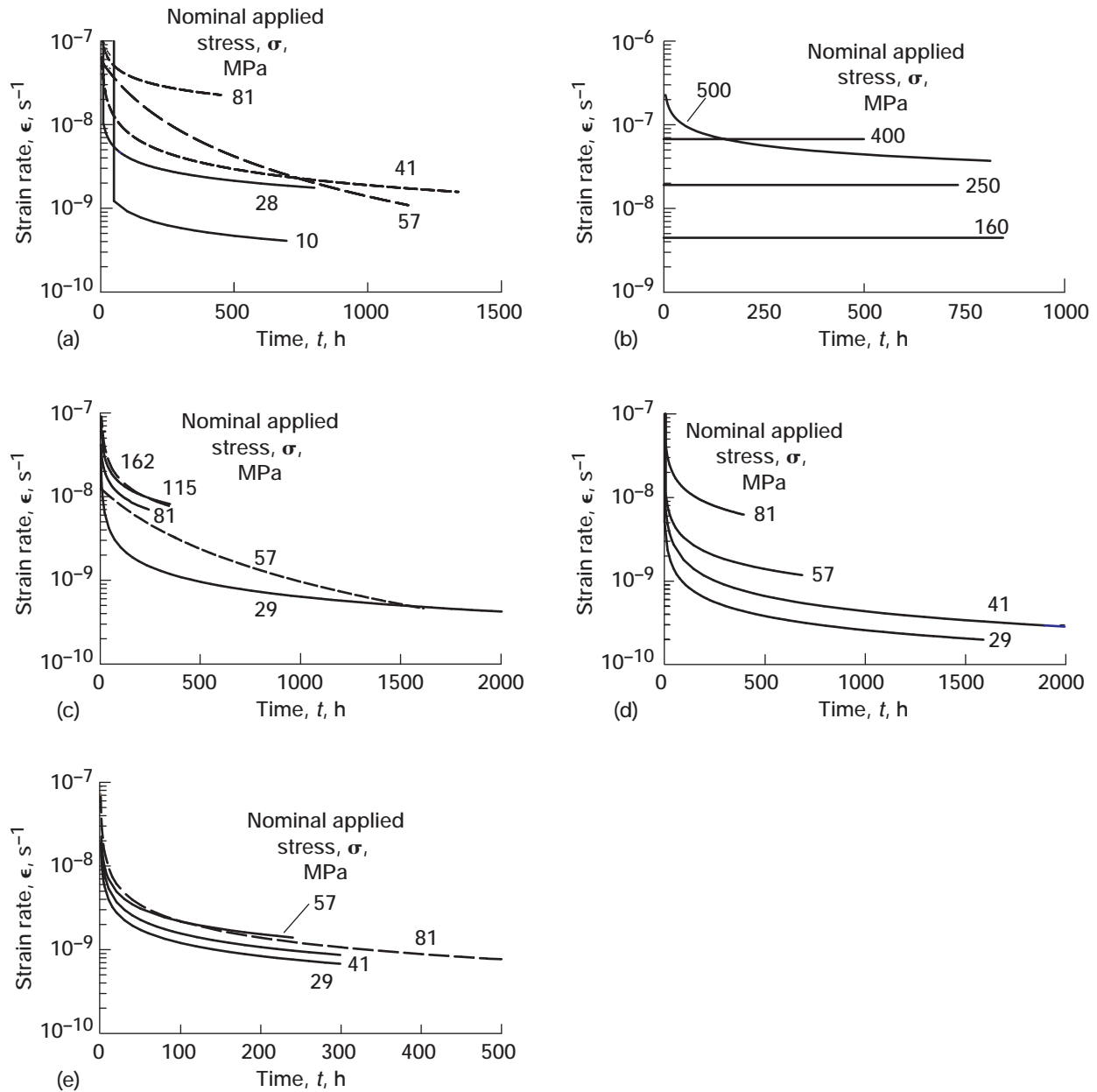


Figure 25.—Nominal creep strain rate as function of time determined for five specimen-loading configurations for NC132 silicon nitride at 1300 °C. (a) Pure tension. (b) Pure compression. (c) Four-point uniaxial flexure. (d) Ball-on-ring biaxial flexure. (e) Ring-on-ring biaxial flexure.

TABLE III. AVERAGE STEADY-STATE STRAIN RATE WITH DIFFERENT LOADINGS FOR NC132 SILICON NITRIDE
AT 1300 °C

Loading	Nominal applied stress, MPa	Strain rate, s ⁻¹				
		At start of testing		At end of testing		Average strain rate, s ⁻¹
		Time, t _{cr} , h	Strain rate, s ⁻¹	Time, t _{cr} , h	Strain rate, s ⁻¹	
Tension	10	100	9.148 10 ⁻¹⁰	700	4.064 10 ⁻¹⁰	6.606 10 ⁻¹⁰
	28	100	4.083 10 ⁻⁹	800	1.755 10 ⁻⁹	2.919 10 ⁻⁹
	41	200	5.250 10 ⁻⁹	1300	1.596 10 ⁻⁹	3.423 10 ⁻⁹
	57	200	1.332 10 ⁻⁸	1100	1.176 10 ⁻⁹	7.248 10 ⁻⁹
	81	50	5.043 10 ⁻⁸	400	2.356 10 ⁻⁸	3.700 10 ⁻⁸
Compression	160	50	4.349 10 ⁻⁹	850	4.349 10 ⁻⁹	4.349 10 ⁻⁹
	250	50	1.866 10 ⁻⁸	750	1.866 10 ⁻⁸	1.866 10 ⁻⁸
	400	50	6.607 10 ⁻⁸	500	6.607 10 ⁻⁸	6.607 10 ⁻⁸
	500	50	9.802 10 ⁻⁸	800	3.654 10 ⁻⁸	6.728 10 ⁻⁸
	630	----	-----	----	-----	-----
Uniaxial flexure	29	200	1.643 10 ⁻⁹	2000	4.224 10 ⁻¹⁰	1.033 10 ⁻⁹
	57	400	2.984 10 ⁻⁹	1600	4.647 10 ⁻¹⁰	1.724 10 ⁻⁹
	81	25	2.010 10 ⁻⁸	220	7.450 10 ⁻⁹	1.378 10 ⁻⁸
	115	5	2.697 10 ⁻⁸	320	8.453 10 ⁻⁹	1.771 10 ⁻⁸
	162	25	3.544 10 ⁻⁸	320	8.016 10 ⁻⁹	2.173 10 ⁻⁸
Ball-on-ring biaxial flexure	29	400	4.368 10 ⁻¹⁰	1600	2.002 10 ⁻¹⁰	3.185 10 ⁻¹⁰
	41	400	7.680 10 ⁻¹⁰	2000	2.784 10 ⁻¹⁰	5.277 10 ⁻¹⁰
	57	200	2.297 10 ⁻⁹	700	1.176 10 ⁻⁹	1.737 10 ⁻⁹
	81	200	4.281 10 ⁻⁹	400	2.973 10 ⁻⁹	3.627 10 ⁻⁹
Ring-on-ring biaxial flexure	29	100	1.202 10 ⁻⁹	300	6.783 10 ⁻¹⁰	9.402 10 ⁻¹⁰
	41	100	1.562 10 ⁻⁹	300	8.648 10 ⁻¹⁰	1.213 10 ⁻⁹
	57	100	2.178 10 ⁻⁹	240	1.397 10 ⁻⁹	1.788 10 ⁻⁹
	81	100	2.168 10 ⁻⁹	500	7.643 10 ⁻¹⁰	1.466 10 ⁻⁹

Nominal Creep Strain Rate Versus Nominal Applied Stress

Numerous models to describe creep strain rate as a function of applied stress have been proposed. In this section, some representative models such as power-law, hyperbolic sine, and step and redistribution models will be reviewed and applied to the experimental data. Creep strain rates in steady state as a function of nominal applied stress have been well represented for many ceramic materials with the conventional power-law Norton-Arrhenius relation (ref. 46):

$$\dot{\epsilon} = A\sigma^N e^{-Q/RT} \quad (14)$$

where A and N are the creep parameters, Q is the activation energy, R is the gas constant, and T is temperature. The parameter N is also known as the stress exponent for creep. The creep parameters A and N are evaluated by a linear regression analysis from the $\log \dot{\epsilon}$ -versus- $\log \sigma$ plot. Some ceramic materials, however, have shown poor applicability of the power-law formulation (refs. 47 and 48). Other models have been suggested to better represent creep strain rate responses for them, particularly for silicon nitrides in tension.

A hyperbolic sine model describing creep strain rate as following the hyperbolic sine function of applied stress (refs. 47, 49, and 50) was used by Hazine and White (ref. 50), who applied an asymmetric flow surface to account for different creep behavior in tension and in compression. An isotropic hardening variable was also employed to describe the continuous drop in creep strain rate with deformation. The resulting strain rate is expressed as

$$\dot{\epsilon} = A' \sinh(\alpha\sigma) e^{(-Q/RT)} \quad (15)$$

where A' and α are parameters to be determined. When $\alpha\sigma \geq 2$, $\sinh(\alpha\sigma) \approx 0.5e^{\alpha\sigma}$, simplify the above equation as

$$\dot{\epsilon} = \beta e^{\alpha\sigma} \quad (16)$$

where $\beta = 0.5A'e^{-Q/RT}$. This simplified expression is virtually the same as the conventional exponential creep representation (ref. 51). In the $\ln \dot{\epsilon}$ -versus- σ plot, the slope and intercept of the curve correspond to α and $\ln \beta$, respectively. Ding, Liu, and Brinkman (ref. 52) also proposed a similar approach using the hyperbolic sine function. The step model of solution-precipitation creep in which the nucleation of new surface steps on certain planes in silicon nitrides controls creep strain rate is as follows (ref. 53):

$$\dot{\epsilon} = \frac{A''}{T} e^{-Q/RT} \sigma^{2/3} e^{-L/(RT\sigma)} \quad (17)$$

where L is a term pertaining to the height of the grain-boundary step and the energy of the step per unit length. Taking a natural logarithm on both sides of equation (17) gives

$$\ln \dot{\epsilon} = \alpha' + \frac{2}{3} \ln \sigma - \beta' \frac{1}{\sigma} \quad (18)$$

where $\alpha' = \ln((A''/T)e^{-Q/RT})$ and $\beta' = L/RT$. The parameters α' and β' can be estimated using a functional-fit analysis.

Recently, a redistribution model has been suggested for the tensile creep of silicon nitride (refs. 54 and 55). This model describes the dependence of the strain rate on applied stress as arising from the kinetics of the redistribution of silicate material from growing cavities throughout the internal volume surrounding them. The model is expressed as

$$\dot{\epsilon} = A^* e^{-Q/RT} \sigma e^{\phi \sigma} \quad (19)$$

where ϕ is a term associated with the density of potential sites for the formation of the cavity. Taking the logarithm on both sides of the equation yields

$$\ln \dot{\epsilon} = \alpha'' + \ln \sigma + \phi \sigma \quad (20)$$

where $\alpha'' = \ln(A^* e^{-Q/RT})$. The parameters α'' and ϕ can be estimated using a functional-fit analysis. In addition to the models already mentioned, a power-law expression using two stress exponents at high and low applied stresses has been proposed for smooth connection between the high-stress and low-stress regions (ref. 56).

A summary of nominal creep strain rate as a function of nominal applied stress using the above four models is presented in figure 26. Note that the data on ring-on-ring biaxial flexure were not included in this figure; this information was produced during a test period of less than 300 h and cannot be compared with data obtained over a longer period. As can be seen in the figure, there was no significant difference in curve fitting between the power-law, hyperbolic sine, and redistribution models. The hyperbolic sine model in particular yields almost the same result as the redistribution model. The power-law model shows a somewhat worse fit to the tension data at high stress, not revealing the actual curvature in the data. Similarly, the step model also gives a worse fit to the tension data, but gives a reasonably good fit to other loading configurations. It should be noted that the models employed here were developed primarily for pure tension loading. Hence, strictly speaking, it is questionable whether the models would be applicable for other than tension loading, since the creep mechanism may vary in different loading configurations.

In view of its mathematical simplicity, the conventional power-law model has been widely used for decades regardless of the type of loading (tension, compression, or flexure) for a quantitative description of the creep behavior of most advanced ceramic materials. The power-law model can provide a convenient, direct assessment of creep response to different variables such as material, specimen-loading configurations, temperature, and environment. The stress exponent N in the power-law model, determined by using equation (14) together with the experimental data, was $N = 1.72 \pm 0.34$ for tension, 2.51 ± 0.36 for compression, 2.01 ± 0.45 for uniaxial flexure, and 2.49 ± 0.28 for ball-on-ring biaxial flexure. The corresponding correlation coefficients (r_{coef}) were all greater than 0.931. The overall stress exponents, ranging from $N = 1.72$ in tension to $N = 2.51$ in compression, did not vary significantly with specimen-loading configurations. By contrast, for a given nominal applied stress, the magnitude of the nominal strain rate decreased in order from tension, where it was highest, to uniaxial flexure, ball-on-ring biaxial flexure, and

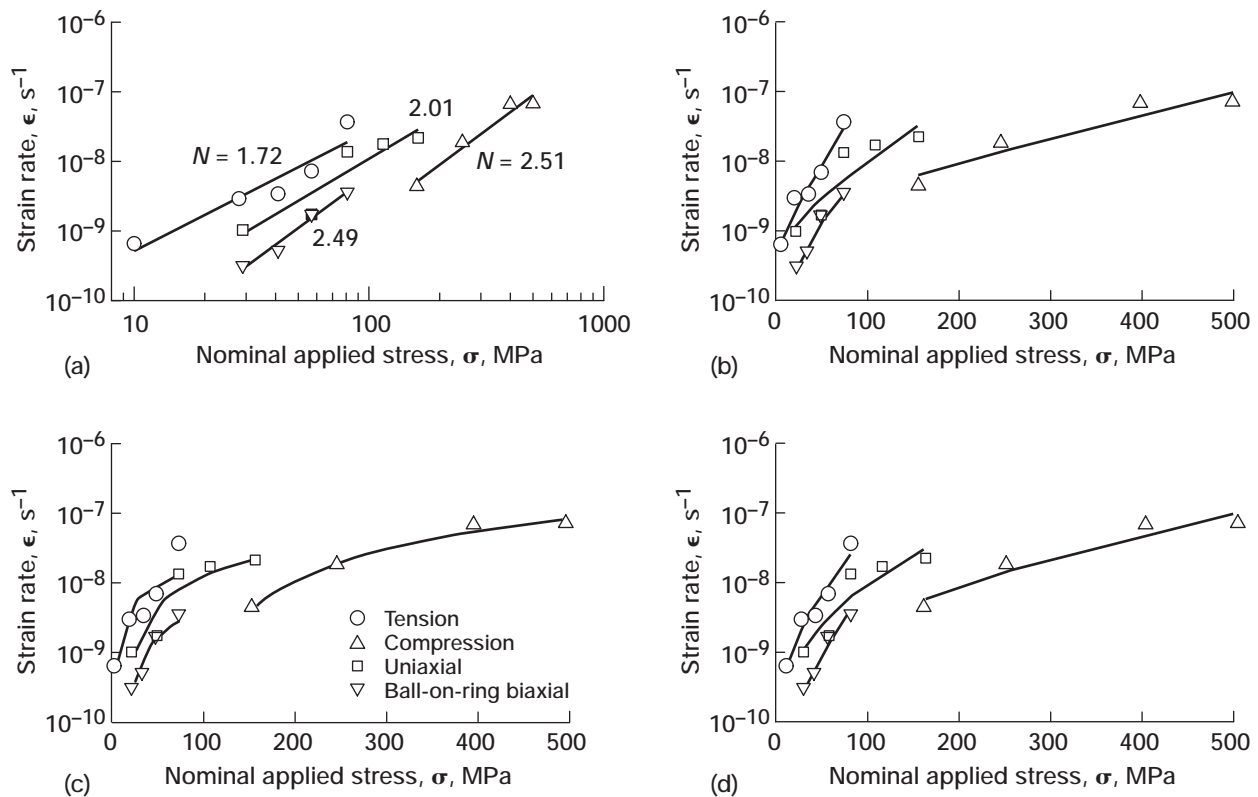


Figure 26.—Nominal creep strain rate as function of nominal applied stress for four specimen-loading configurations for NC132 silicon nitride at 1300 °C and fitted to four creep models. (a) Power-law (Norton) model. $N = 1.72$ to $N = 2.51$. (b) Hyperbolic sine model. (c) Step model. (d) Redistribution model.

compression, where it was lowest. Uniaxial and biaxial flexure fall between tension and compression because flexure is a combination of the two. The strain rate for uniaxial flexure was greater than that for biaxial flexure, which is ascribed to the greater constraint imposed on the biaxial flexure configuration.

The negligible difference in stress exponent N between the four loading configurations implies that the mechanisms associated with creep of this material would not be significantly different with any specimen-loading configuration. It was generally observed that dislocation and cavitation mechanisms yield values of $N \approx 3 - 6$; diffusion creep and/or viscous flow of the glassy phase yields the value of $N \approx 1$; and grain-boundary sliding results in $N \approx 2$ (refs. 57 to 59). Cannon and Langdon (ref. 57) showed that many silicon nitrides exhibited a stress exponent of $N \approx 2$ regardless of loading type. The mechanism was elaborated as grain-boundary sliding with intergranular cavitation. Based on this categorization, grain-boundary sliding could be the creep mechanism responsible for this in NC132 silicon nitride. Detailed microstructural examinations of crept specimens using SEM, TEM, and/or density measurements will be needed to determine the governing creep mechanism.

Although the stress exponent was not significantly different between tension and compression, the difference in strain (and strain rate) between the two for a given applied stress was significant. The strain in tension was about 1.5 to 2 orders of magnitude larger than that in compression, if the compression data are extrapolated toward lower stresses. This difference in creep strain between tension and compression eventually results in a neutral axis shift toward the compression side of a flexure beam specimen. It was reported that flexure beam specimens of many ceramic materials exhibit a neutral axis shift for equilibrium because of the difference in creep strain, often accompanied by appreciable void and/or cavitation formation on the tension side (refs. 1, 3, 38, 39, 60, and 61). Because of this asymmetric creep behavior, the data determined from flexure creep testing are considered inappropriate for use as design parameters of structural ceramic components. Separate tension and compression data must be determined to completely characterize creep behavior of a material so that creep deformation and rupture of structural components in service can be predicted. Recent studies using the data generated in this work demonstrate that with individual tensile and compressive creep data and taking into account the neutral-axis shift, a reasonable prediction of creep deformation of flexure beam specimens can be obtained with the CARES/Creep design code.

Generation of the creep data base using NC132 silicon nitride is still in progress. The data base will be used to predict creep deformation under multiaxial stress states using the CARES/Creep code. More exact stress distributions in flexure (uniaxial or biaxial) for a given time will be determined using both pure tensile and pure compressive creep data with an appropriate finite-element code. Work is also planned to extend this testing procedure to other advanced monolithic ceramics such as alumina and other silicon nitrides for more complete code verification and data base generation. Other recent information on this topic is available (ref. 62).

CONCLUSIONS

Creep testing of a hot-pressed silicon nitride (NC132) was conducted using five specimen-loading configurations at 1300 °C in air. The specimen-loading configurations used in this study were pure tension, pure compression, four-point uniaxial flexure, ball-on-ring biaxial flexure, and ring-on-ring biaxial flexure. Creep deformation was determined as a function of time for typically four to six applied loads. Test times ranged from 100 to 2000 h, depending on the type and magnitude of applied loading. Except for compressive creep, nominal strain rate decreased gradually with time, resulting in a less-defined steady-state condition. The magnitude and rate of nominal creep strain for a given nominal applied stress were greatest in tension, least in compression, and intermediate in uniaxial and biaxial flexure.

Four creep models—power-law, hyperbolic sine, step, and redistribution—were applied to the experimental data. All the models gave a reasonable data fit; it is unclear which would be most appropriate for the NC132 material. The conventional power-law model showed an overall stress exponent of about 2 (ranging from 1.72 to 2.51) irrespective of specimen-loading configuration. This ongoing experimental work will continue to generate a creep data base as well as to verify the NASA Glenn-developed CARES/Creep design code.

WORK IN PROGRESS

The paper “Creep Life Prediction of a Silicon Nitride with Multiple Specimen Configurations” was presented by Lynn Powers with Sung Choi, John Gyekenyesi, and D.A. Gasparini at the 23rd Annual Cocoa Beach Conference (Paper No. C-109-99, Cocoa Beach, FL, January, 1999) of the American Ceramic Society.

REFERENCES

1. Wiederhorn, S.M., et al.: Damage-Enhanced Creep in a Siliconized Silicon Carbide: Phenomenology. *Am. Cer. Soc. J.*, vol. 71, 1988, pp. 602–608.
2. Ferber, M.K.; Jenkins, M.G.; and Tennerly, V.J.: Comparison of Tension, Compression, and Flexure Creep for Alumina and Silicon Nitride Ceramics. *Ceram. Eng. Sci. Proc.*, vol. 11, 1990, pp. 1028–1045.
3. Chuang, T.J.: Estimation of Power-Law Creep Parameters from Bend Test Data. *J. Mater. Sci.*, vol. 21, 1986, pp. 165–175.
4. Quinn, G.D.; and Quinn, J.B.: Slow Crack Growth in Hot-Pressed Silicon Nitride. *Fracture Mechanics of Ceramics*, vol. 6, Plenum Press, New York, NY, 1983, pp. 603–636.
5. Choi, S.R.; and Salem, J.A.: Effect of Preloading on Fatigue Strength in Dynamic Fatigue Testing of Ceramic Materials at Elevated Temperatures. *Ceram. Eng. Sci. Proc.*, vol. 16, no. 4, 1995, pp. 87–94.
6. Jadaan, O.M.; Powers, L.M.; and Gyekenyesi, J.P.: Creep Life Prediction of Ceramic Components Subjected to Transient Tensile and Compressive Stress States. *ASME Paper 97-GT-319*, 1997.
7. Powers, L.M.; Jadaan, O.M.; and Gyekenyesi, J.P.: Creep Life of Ceramic Components Using a Finite-Element-Based Integrated Design Program. *J. Eng. Gas Turbines Power*, vol. 120, 1998, pp. 162–171.
8. Monkman, F.; and Grant, N.: An Empirical Relationship Between Rupture Life and Minimum Creep Rate in Creep-Rupture Tests. *Proc. American Society for Testing Materials*, vol. 56, 1956, pp. 593–620.
9. Bratton, R.J., et al.: Brittle Materials Design, High Temperature Gas Turbine Material Technology. *AMMRC-CTR-76-32*, vol. 1, Army Materials and Mechanics Research Center, 1976.

10. Govila, R.K.: Ceramic Life Prediction Parameters. AMMRC-TR 80-18, Army Materials and Mechanics Research Center, 1980.
11. Standard Test Method for Dynamic Young's Modulus, Shear Modulus, and Poisson's Ratio for Advanced Ceramics by Impulse Excitation of Vibration. ASTM C1259-98, 1998.
12. Standard Test Method for Vickers Indentation Hardness of Advanced Ceramics. ASTM C1327-99, 1999.
13. Standard Test Methods for Fracture Toughness of Advanced Ceramics at Ambient Temperatures. ASTM C1421-99, 1999.
14. Standard Test Method for Flexural Strength of Advanced Ceramics at Ambient Temperature. ASTM C1161-94, 1996.
15. Standard Test Method for Determination of Slow Crack Growth Parameters of Advanced Ceramics by Constant Stress-Rate Flexural Testing at Ambient Temperature. ASTM C1368-99, 1999.
16. Choi, S.R.; Powers, L.M.; and Nemeth, N.N.: Slow Crack Growth Behavior and Life/Reliability Analysis of 96 wt % Alumina at Ambient Temperature With Various Specimen/Loading Configurations. NASA TM-210206, 2000.
17. Carroll, D.F.; Wiederhorn, S.M., and Roberts, D.E.: Technique for Tensile Creep Testing of Ceramics. Am. Cer. Soc. J., vol. 72, 1989, pp. 1610-1614.
18. Choi, S.R.; Salem, J.A.; and Palko, J.L.: Comparison of Tension and Flexure to Determine Fatigue Life Prediction Parameters at Elevated Temperatures. ASTM STP-1201, 1994, pp. 98-111.
19. Standard Test Method for Elevated Temperature Tensile Creep Strain, Creep Strain Rate, and Creep Time-to-Failure for Advanced Monolithic Ceramics, ASTM 1291-95e1, 1995.
20. Birch, J.M., et al.: The Influence of Stress Distribution on the Deformation and Fracture Behaviour of Ceramic Materials Under Compression Creep Conditions. J. Mater. Sci., vol. 11, 1976, pp. 1817-1825.
21. Debschütz, K.D., et al.: Critical Evaluation of the Compression Creep Test. J. Am. Ceram. Soc., vol. 76, no. 10, 1993, pp. 2468-2474.
22. Standard Test Methods of Compression Testing of Metallic Materials at Room Temperature, ASTM E9-89ae1, 2000.
23. Page, R.A., et al.: Creep Cavitation in Liquid-Phase-Sintered Alumina. J. Am. Ceram. Soc., vol. 70, no. 3, 1987, pp. 137-145.
24. Parthasarathy, T.A.; Mah, T.I.; and Keller, K.: Creep Mechanism of Polycrystalline Yttrium Aluminum Garnet. J. Am. Ceram. Soc., vol. 75, no. 7, 1992, pp. 1756-1759.
25. Lange, F.F.; Davis, B.I.; and Clarke, D.R.: Compressive Creep of $\text{Si}_3\text{N}_4/\text{MgO}$ Alloys, Part 1—Effect of Composition. J. Mater. Sci., vol. 15, 1980, pp. 601-618.
26. Corman, G.S.: Creep of Beryllia Crystals. Am. Cer. Soc., J., vol. 75, 1992, pp. 71-76.
27. Martinez-Fernandez, J., et al.: High-Temperature Creep of Yttria-Stabilized Zirconia Single Crystals. Am. Cer. Soc. J., vol. 73, 1990, pp. 2452-2456.
28. Standard Test Method for Flexural Strength of Advanced Ceramics at Elevated Temperatures, ASTM C1211-98a, 1998.
29. Shetty, D.K.; et al.: Biaxial Flexure Tests for Ceramics. Am. Cer. Soc. Bul., vol. 59, 1980, pp. 1193-1197.
30. De With, G. and Wagemans, H.H.M.: Ball-on-Ring Test Revisited. J. Am. Ceram. Soc., vol. 72, no. 8, 1989, pp. 1538-1541.
31. Atkins, A.G.; Silverio, A.; and Tabor, D.: Indentation Hardness and the Creep of Solids. JIME vol. 94, 1966, pp. 369-378.
32. Chu, S.N.G.; and Li, J.C.M.: Impression Creep: A New Creep Test, J. Mater. Sci., vol. 12, 1977, pp. 2200-2208.
33. Wilshaw, T.R.: Measurements of Tensile Strength of Ceramics. J. Am. Ceram. Soc., vol. 51, 1968, p. 111.
34. Quinn, G.D. and Wirth, G.: Multiaxial Strength and Stress Rupture of Hot Pressed Silicon Nitride. J. Eur. Ceram. Soc., vol. 6, no. 3, 1990, pp. 169-177.
35. Choi, S.R., et al.: High Temperature Slow Crack Growth of Si_3N_4 Specimens Subjected to Uniaxial and Biaxial Dynamic Fatigue Loading Conditions. Ceram. Eng. Sci. Proc., vol. 16, no. 4, 1995, pp. 509-517.
36. Choi, S.R.; and Salem, J.A.: Free-Roller Versus Fixed-Roller Fixtures in Flexure Testing of Advanced Ceramic Materials. Ceram. Eng. Sci. Proc., vol. 17, no. 3, pp. 69-77.
37. Choi, S.R.; and Salem, J.A.: Error in Flexure Testing of Advanced Ceramics under Cyclic Loading. Ceram. Eng. Sci. Proc., vol. 18, no. 3, 1997, pp. 495-502.

38. Salem, J.A.; and Choi, S.R.: Creep Behavior of Silicon Nitride Determined from Curvature and Neutral Axis Shift Measurements in Flexure Tests. ASTM STP-1201, 1994, pp. 84-97.
39. Sheldon, B.W.; and Danforth, S.C. eds.: Silicon-Based Structural Ceramics, Ceramic Transactions, American Ceramic Society, Westerville, OH, vol. 42, 1994.
40. Kirstein, A.F.; and Woolley, R.M.: Symmetrical Bending of Thin Circular Elastic Plates on Equally Spaced Point Supports. Eng. and Instrumentation, vol. 71C, 1967, pp. 1-10.
41. Timoshenko, S.P.; and Woinowsky-Krieger, S.: Theory of Plates and Shell. Second ed., McGraw-Hill, New York, NY, 1959.
42. Manley, M.E., et al.: Four Point and Biaxial Flexure Strength of PZT Ceramics: A Probabilistic Approach. Ceram. Eng. Sci. Proc., vol. 15, no. 5, 1994, pp. 885-894.
43. Kao, R.; Perrone, N; and Capps, W.: Large-Deflection Solution of the Coaxial-Ring-Circular-Glass-Plate Flexure Problem. Am. Cer. Soc. J., vol. 54, 1971, pp. 566-571.
44. Cranmer, D.C., et al.: Creep and Creep Rupture of HIPed Si_3N_4 . Ceram. Eng. Sci. Proc., vol. 12, 1991, pp. 1862-1872.
45. Wilkinson, D.S.: Creep Mechanisms in Multiphase Ceramic Materials. Am. Cer. Soc. J., vol. 81, no. 2, 1998, pp. 275-299.
46. Norton, F.H.: The Creep of Steel at High Temperatures. McGraw Hill, New York, NY, 1929.
47. Gasdaska, C.J.: Tensile Creep in an In Situ Reinforced Silicon Nitride. J. Am. Ceram. Soc., vol. 77, no. 9, 1994, pp. 2408-2418.
48. Luecke, W.E., et al.: Cavitation Contributes Substantially to Tensile Creep in Silicon Nitride. Am. Cer. Soc. J., vol. 78, no. 8, 1995, pp. 2085-2096.
49. Contributions to the Mechanics of Solids Dedicated to Stephen Timoshenko by His Friends on the Occasion of His 60th Birthday Anniversary. MacMillan, New York, NY, 1938.
50. Hazine, R.M.; and White, C.S.: Multiaxial Internal Variable Modeling of the Creep Deformation and Fracture of an Advanced Silicon Nitride. Ceram. Eng. Sci. Proc., vol. 18, no. 3, 1997, pp. 455-465.
51. Söderberg, C.R.: Interpretation of Creep Tests for Machine Design. ASME Trans., vol. 58, no. 8, 1936, pp. 733-743.
52. Ding, J.L.; Liu, K.C.; Brinkman, C.R.: Comparative Study of Existing and Newly Proposed Models for Creep Deformation and Life Prediction of Si_3N_4 . ASTM STP-1201, 1994, pp. 62-83.
53. Li, C.-W. and Reidinger, F.: Microstructure and Tensile Creep Mechanisms of an In situ Reinforced Silicon Nitride. Acta Mater., vol. 45, no. 1, 1997, pp. 407-421.
54. Krause, R.F., et al.: Tensile Creep and Rupture Silicon Nitride. Am. Cer. Soc. J., vol. 82. no. 5, 1999, pp. 1233-1241.
55. Luecke, W.E.; and Wiederhorn, S.M.: A New Model for Tensile Creep of Silicon Nitride. J. Am. Ceram. Soc., vol. 82, no. 10, 1999, pp. 2769-2847.
56. Menon, M.N., et al.: Creep and Stress Rupture Behavior of an Advanced Silicon Nitride: Part II, Creep Rate Behavior. J. Am Ceram. Soc., vol. 77, no. 5, 1994, pp. 1228-1234.
57. Cannon, W.R.; and Langdon, T.G.: Creep of Ceramics-1: Mechanical Characteristics. J. Mater. Science, vol. 18, no. 1, 1983, pp. 1-50.
58. Cannon, W.G. and Langdon, T.G.: Creep of Ceramics-2: An Examination of Flow Mechanisms. J. Mater. Sci., vol. 23, 1988, pp. 1-20.
59. Munz, D.; and Fett, T.: Ceramics. Springer-Verlag, Berlin, Germany, 1999.
60. Jakus, K.; and Wiederhorn, S.M.: Creep Deformation of Ceramics in Four-Point Bending. Am. Cer. Soc. J., vol. 71, no. 10, 1988, pp. 832-836.
61. Ferber, M.K.; Jenkins, M.G.; and Tennerly, V.J.: Comparison of Tension, Compression, and Flexure Creep for Alumina and Silicon Nitride Ceramics. Ceram. Eng. Sci. Proc., vol. 11, 1990, pp. 1028-1045.
62. Choi, S.R.; Powers, L.M.; and Gyekenyesi, J.P.: Creep Behavior of a Silicon Nitride With Various Specimen/ Loading Configurations, and Creep Prediction Using the CARES/Creep Program. Proceedings of the First China International Conference on High-Performance Ceramics (CICC-1), D.S. Yan and Z.D. Guan, eds., (Beijing, China), Oct. 1998, pp. 612-615.

REPORT DOCUMENTATION PAGE			Form Approved OMB No. 0704-0188	
Public reporting burden for this collection of information is estimated to average 1 hour per response, including the time for reviewing instructions, searching existing data sources, gathering and maintaining the data needed, and completing and reviewing the collection of information. Send comments regarding this burden estimate or any other aspect of this collection of information, including suggestions for reducing this burden, to Washington Headquarters Services, Directorate for Information Operations and Reports, 1215 Jefferson Davis Highway, Suite 1204, Arlington, VA 22202-4302, and to the Office of Management and Budget, Paperwork Reduction Project (0704-0188), Washington, DC 20503.				
1. AGENCY USE ONLY (Leave blank)		2. REPORT DATE November 2000		3. REPORT TYPE AND DATES COVERED Technical Memorandum
4. TITLE AND SUBTITLE Silicon Nitride Creep Under Various Specimen-Loading Configurations			5. FUNDING NUMBERS WU-910-30-11-00	
6. AUTHOR(S) Sung R. Choi and Frederic A. Holland				
7. PERFORMING ORGANIZATION NAME(S) AND ADDRESS(ES) National Aeronautics and Space Administration John H. Glenn Research Center at Lewis Field Cleveland, Ohio 44135-3191			8. PERFORMING ORGANIZATION REPORT NUMBER E-12223	
9. SPONSORING/MONITORING AGENCY NAME(S) AND ADDRESS(ES) National Aeronautics and Space Administration Washington, DC 20546-0001			10. SPONSORING/MONITORING AGENCY REPORT NUMBER NASA TM-2000-210026	
11. SUPPLEMENTARY NOTES Sung R. Choi, Ohio Aerospace Institute, 22800 Cedar Point Road, Brook Park, Ohio 44142; and Frederic A. Holland, NASA Glenn Research Center. Responsible person, Frederic A. Holland, organization code 5920, 216-433-8367.				
12a. DISTRIBUTION/AVAILABILITY STATEMENT Unclassified - Unlimited Subject Categories: 07 and 39 This publication is available from the NASA Center for AeroSpace Information, 301-621-0390.			12b. DISTRIBUTION CODE	
13. ABSTRACT (Maximum 200 words) Extensive creep testing of a hot-pressed silicon nitride (NC132) was performed at 1300 °C in air using five different specimen-loading configurations: pure tension, pure compression, four-point uniaxial flexure, ball-on-ring biaxial flexure, and ring-on-ring biaxial flexure. This paper reports experimental results as well as test techniques developed in this work. Nominal creep strain and its rate for a given nominal applied stress were greatest in tension, least in compression, and intermediate in uniaxial and biaxial flexure. Except for the case of compression loading, nominal creep strain generally decreased with time, resulting in a less-defined steady-state condition. Of the four creep formulations—power-law, hyperbolic sine, step, and redistribution—the conventional power-law formulation still provides the most convenient and reasonable estimation of the creep parameters of the NC132 material. The data base to be obtained will be used to validate the NASA Glenn-developed design code CARES/Creep (ceramics analysis and reliability evaluation of structures and creep).				
14. SUBJECT TERMS Advanced ceramics; Silicon nitride; Creep; Creep testing			15. NUMBER OF PAGES 36	
			16. PRICE CODE A03	
17. SECURITY CLASSIFICATION OF REPORT Unclassified	18. SECURITY CLASSIFICATION OF THIS PAGE Unclassified	19. SECURITY CLASSIFICATION OF ABSTRACT Unclassified	20. LIMITATION OF ABSTRACT	